

The characterization of tandem and corrugated wings

Yongsheng Lian ^{*}, Timothy Broering, Kyle Hord, Russell Prater

Mechanical Engineering Department, University of Louisville, Louisville, KY 40292, USA



ARTICLE INFO

Available online 16 October 2013

Keywords:

Tandem wing
Corrugated wing
CFD
Leading edge vortex
Wing vortex interaction

ABSTRACT

Dragonfly wings have two distinct features: a tandem configuration and wing corrugation. Both features have been extensively studied with the aim to understand the superior flight performance of dragonflies. In this paper we review recent development of tandem and corrugated wing aerodynamics. With regards to the tandem configuration, this review will focus on wing/wing and wing/vortex interactions at different flapping modes and wing spacing. In addition, the aerodynamics of tandem wings under gusty conditions will be reviewed and compared with isolated wings to demonstrate the gust resistance characteristics of flapping wings. Regarding corrugated wings, we review their structural and aerodynamic characteristics.

© 2013 Elsevier Ltd. All rights reserved.

Contents

1. Introduction	42
1.1. Micro-air vehicles	42
1.2. Flapping wing aerodynamics	42
1.3. Tandem wing aerodynamics	43
1.3.1. Phase angle and force production in hovering motion	45
1.3.2. Phase angle and force production in forward flight	45
1.3.3. Vortex and wing interaction	45
1.3.4. Effect of wing spacing	45
1.4. Wind gust and flapping wings	45
1.5. Corrugated wings	46
2. Numerical methods	47
3. Tandem wing aerodynamics	48
3.1. Effect of phase angle	48
3.1.1. Aerodynamic forces	49
3.1.2. Flow visualization results	53
3.2. Effect of wing spacing	57
3.2.1. Aerodynamic force results	57
3.2.2. Flow visualization results	57
3.2.3. Effect of vortex interaction on CP	58
3.2.4. Effect of phase angle vs. spacing	58
3.3. Conclusions	60
4. Tandem wing and wind gust	61
4.1. Single wing results	62
4.2. Tandem wing results	63
4.2.1. Case 1: Two stationary wings in tandem configuration	63
4.2.2. Case 2: Flapping fore-wing and stationary hind-wing	64
4.2.3. Case 3: Stationary fore-wing and flapping hind-wing	64
4.3. Conclusions	64
5. Corrugated wing performance	65

* Corresponding author. Tel.: +1 502 852 0804.

E-mail address: yongshenglian@gmail.com (Y. Lian).

5.1. Effect of angle of attack	65
5.2. Effects of corrugation	65
5.3. Structural analysis	66
5.4. Conclusions	66
6. Conclusions	67
References	67

1. Introduction

1.1. Micro-air vehicles

The success in recent years of unmanned air vehicles, or UAV's has generated an interest in research efforts to create similar vehicles of reduced size. These micro-air vehicles (MAVs) are small, autonomous air vehicles that are of interest for a variety of military and civilian applications [1–4]. The term MAV is typically used to define an air vehicle that has no length dimension greater than 6 in. and a gross takeoff weight (GTOW) of less than 200 g. Such tiny air vehicles would be capable of operating in confined spaces, making them ideal for missions in urban environments. Missions of primary interest include reconnaissance and surveillance, target detection, and search and rescue. Some examples of MAV designs include the Black Widow, designed by Aeroenvironment [5], and the Microbat by Caltech [6] as shown in Fig. 1. The Black Widow is a fixed wing MAV design that has a GTOW of 80 g and is capable of remaining airborne for almost 30 min, while the Microbat is a flapping wing MAV design that has a GTOW of 10 g and is capable of remaining airborne for less than 5 min. MAVs such as these have a number of potential uses, however, designing MAVs similar to these, with extended flight times and high maneuverability, presents a number of challenges.

Due to their small size and slow flight velocity, MAVs operate at low Reynolds numbers, below 100,000, which presents a number of challenging aerodynamic problems such as massive laminar flow separation and laminar-to-turbulent transition. At low Reynolds numbers, flow across the wing is typically laminar and viscous effects become important. Conventional fixed wing aircraft are designed to operate at high Reynolds numbers, well above 100,000, where the flow is turbulent and remains attached. In contrast, laminar flow over the wing separates before the flow becomes turbulent, leading to early stalls. The decreased efficiency, in terms of the lift to drag ratio, of fixed wings at Reynolds numbers below 100,000, is shown in Fig. 2 [7]. All these challenges make designing fixed wing MAVs, aimed for operating over a wide range of angles of attack and extended flight time, challenging. Investigating nature, however, provides an alternative design method. Natural fliers, such as small birds and insects, operate in the same Reynolds number regime as MAVs, producing superior aerodynamic performance through flapping motions.

Understanding the methods birds and insects use to attain high lift performance will provide useful insights in developing more efficient MAV designs. Flapping wings rely heavily on the generation and complex interactions of vortices to provide lift and thrust as opposed to the steady state flow dynamics utilized by fixed wing designs [8–13]. Of particular interest is the role leading edge vortices play in the enhancement of lift and thrust.

1.2. Flapping wing aerodynamics

Flapping wing movement, similar to a bird or insect, is a complicated mix of periodic pitching (rotational motion), plunging (vertical motion) and surging (horizontal motion). The unsteadiness of flapping motions can be characterized by a dimensionless number called the reduced frequency

$$k = \frac{\omega c}{2U} \quad (1)$$

where ω , c , and U are the flapping wing's angular velocity, the wing's reference chord, and the forward flight velocity respectively. The faster the wing flaps, or the slower the flight velocity, the higher value of the reduced frequency, and the greater the increase in unsteady effects. Smaller birds tend to have higher

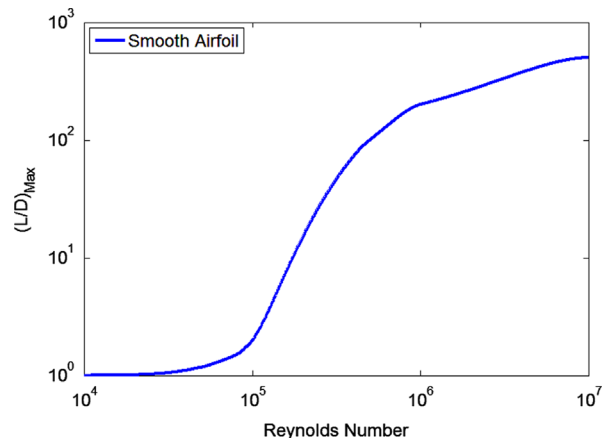


Fig. 2. Lift coefficient vs. Reynolds number for smooth airfoils [7].

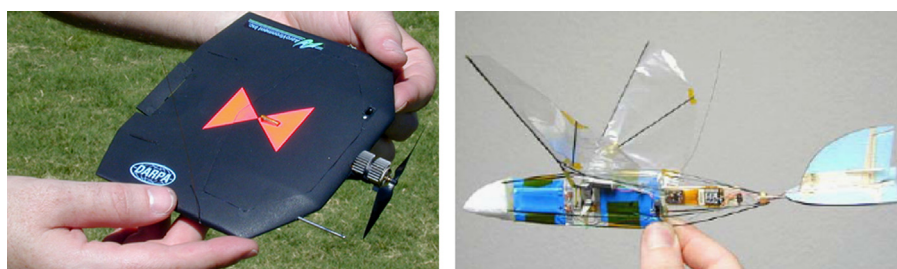


Fig. 1. Two typical MAV designs. The Black Widow [5] on the left and the Microbat [6] on the right.

reduced frequencies than larger birds, indicating that they fly under more unsteady flow conditions [10].

Another useful nondimensional parameter that can be used to characterize flight performance is the Strouhal number

$$St = \frac{2f h_a}{U} \quad (2)$$

where f is the flapping frequency, h_a is flapping amplitude, and U is the forward flight speed. The Strouhal number is often used as a measure of flight efficiency. Studies by Taylor et al. [14] show that the Strouhal number of 42 different species of bats, birds and insects in cruise flight fell within a narrow range of $0.2 < St < 0.4$, with an average value of 0.29. This indicates that the Strouhal number can be used as a guideline for optimizing flapping wing designs for efficiency.

Knoller [15] and Betz [16] are attributed as the first to observe that a plunging airfoil in a moving flow stream produces a net thrust. The relative vertical velocity imparted by the up and downstroke creates an effective angle of attack, which causes the resultant force to be slanted forward, indicating a thrust component. Fig. 3 illustrates this for an airfoil at zero angle of attack.

As described by Knoller [15] and Betz [16], and later demonstrated by Young et al. [17] the plunging airfoil in this figure will generate a net thrust but no lift, since the negative lift component of the upstroke cancels the positive lift component of the downstroke. Lift generation requires that the plunging airfoil have a positive angle of attack. In this case, the effective angle of attack will be greater on the downstroke than the upstroke. Since lift increases with increasing angle of attack, up until a stall, the resultant force on the downstroke will be greater than the resultant force on the upstroke, therefore; the downstroke will produce more thrust than the upstroke and will generate a larger positive lift than the negative lift produced by the upstroke. In this case the plunging airfoil will generate net thrust and lift. The Knoller–Betz model, however; fails to take into account the vortices that are generated and shed as the airfoil is flapped. Recently the Knoller–Betz effect was experimentally and numerically studied by Dohring et al. [12].

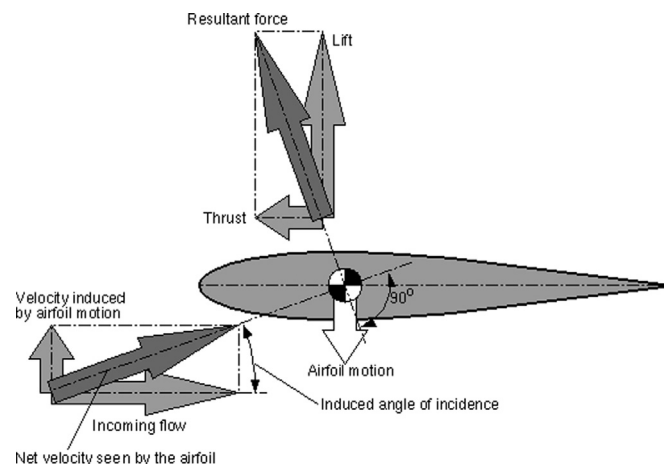


Fig. 3. Induced velocities and resultant forces on a plunging airfoil.

An airfoil undergoing pure pitching is also capable of producing thrust as first shown by Garrick [18]. The pitching frequency must be very high, however; for the thrust production to overcome the drag over the airfoil. This leads to the possibility, as observed in natural fliers, that the most efficient means of propulsion is a combination of pitching and plunging. Of particular interest in this case is what phase angle between pitching and plunging leads to the most efficient thrust generation. Investigations using panel code on a NACA 0012 airfoil pitching about its quarter chord point at an amplitude of 4° have shown that a pitching–plunging mode is most efficient when pitching leads plunging by 90° [19].

1.3. Tandem wing aerodynamics

Both single and tandem wing configurations have been used by nature's flyers (Fig. 4). Studying the unsteady flow interactions between two closely situated wings is far more complex than the case of a single wing; however, two pairs of wings can provide a number of benefits such as increased lift and thrust, and gust resistance [9,20]. Though there are several different ways of configuring two pairs of wings, of primary concern to this review are configurations similar to that of a dragonfly.

Dragonflies are capable flying insects that utilize two pairs of independently actuated wings, with the hind set of wings operating in the wake of the fore set of wings. They are one of the fastest and most maneuverable flying insects, with measured flight speeds of up to 10 m/s and instantaneous accelerations up to 4g's [21]. Tethered dragonflies have even been measured producing up to 20 times their body weight in lift forces [22]. The wing kinematics in free flight is reported by Dong et al. [23]. Their impressive flight capabilities have generated interest in the study of flapping tandem wing configurations as a basis for the design of micro-air vehicles that operate at similar Reynolds numbers.

A significant trait of the tandem wing arrangement is that the hind-wing interacts with the wake of the fore-wing. Experiments by Schmidt have shown that placing a non-flapping hind wing in the wake of a flapping fore-wing almost doubles the propulsive efficiency compared to the fore-wing flapping alone [24]. Similar results were obtained by Bosch through theoretical analysis and by Tuncer and Platzer using CFD analysis [25,26].

Rather than employing a fixed set of hind-wings, dragonflies flap both pairs of wings. Because both pairs of wings are independently actuated, the dragonfly can adjust the phase angle, ψ , between the flapping motion of the fore and hind wings. By observing dragonflies in flight, Alexander noted that they frequently make use of phase shifting; flapping inphase ($\psi=0^\circ$) during takeoff or when undergoing maneuvers and flapping out of phase when in cruising flight [27]. Further observations by Ruppell [28], Azuma and Watanabe [29], and Thomas et al. [30] noticed similar behavior, and it has been postulated that flapping inphase allows for high force production while flapping out of phase allows for increased efficiency, with the hind-wing extracting energy from the wake of the fore-wing [27,31].

In the next we review some important characteristics in tandem wing aerodynamics, namely the phase angle and force



Fig. 4. Single and tandem wing configurations used by nature's flyers.

Table 1

Summary of studies investigating the phase relationship between tandem wings.

Group	Method	Results
Thomas et al. [30]	Smoke visualization/field observation	Counterphase stroke for cruise flight; inphase for high maneuver and escape
Lan [31]	Double Lattice	Increase in thrust and efficiency at some optimum phase angle when hind-wing leads fore-wing
Lan and Sun [37]	2D computational (forward flight)	Increase in thrust at 90°, decrease in resultant at 90° and 180°, resultant unchanged at 0°
Sun and Lan [36]	3D computational (hovering)	Interaction between fore and hind wings detrimental, reduced lift around both fore and hind wings
Sun and Huang [44]	3D computational (Forward Flight)	Lift and thrust forces decreased when fore-wing leads hind-wing, lift and thrust forces mostly unchanged when hind-wing leads fore-wing
Usherwood and Lehmann [32]	Experimental (hovering)	Interaction between fore and hind wings decreases lift, 22% greater efficiency than isolated wings when hind-wing leads fore-wing by 90°
Broering et al. [46]	2D computational (forward flight)	Power coefficient and resultant force coefficient at different phases
Broering and Lian [50]	2D computational (forward flight)	The effects of phase and wing space
Rival et al. [48]	Experimental	Fore-wing is not affected by the hind-wing
Kumar and Hu [51]	Experimental	When spacing is less than 0.15 chord tandem wings act like a single wing; when spacing is more than 2 chord wings act like separated wings
Schmidt [24]	Experimental	Placing a fixed hind-wing in the wake of a flapping fore-wing doubles the propulsive efficiency
Bosch [25]	Theoretical	The propulsive efficiency is increased when a fixed hind-wing is placed in the wake of a flapping fore wing
Tuncer and Platzer [26]	2D computational (forward flight)	A fixed hind-wing, placed in the wake of a flapping fore-wing, can increase propulsive efficiency
Alexander [27]	Biological observation	Dragonflies flap inphase during high force maneuvers and flap out of phase during cruising flight
Ruppell [28]	Biological observation	Dragonflies make use of phase shifting during winged flight
Azuma and Watanabe [29]	Biological observation	Phase shifting between the fore and hind wings is utilized by dragonflies during flight
Wang and Russell [35]	2D computational (hovering)	Maximum resultant force achieved when flapping inphase. Maximum efficiency achieved when flapping with a phase angle near 180°
Akhtar [43]	2D computational (forward flight)	At certain phase angles the propulsive efficiency of a tandem configuration is nearly double that of a single wing
Warkentin and Delaurier [39]	Experimental (forward flight)	Tandem configuration has higher propulsive efficiency than single wing at certain phase angles
Wang and Sun [45]	3D computational (forward flight)	The resultant force coefficient of the tandem configuration at different phase angles is noticeably lower than that of a single wing
Saharon and Luttgess [40–42]	Experimental	Adjusting the phase angle affects the vortex interactions between the fore and hind wings
Maybury and Lehmann [33]	Experimental (hovering)	The phase angle at which peak lift production occurs changes as the hind-wing is moved closer to the fore-wing
Lim and Tay [49]	2D computational (forward flight)	At certain spacing and phase angle the tandem wing performs better than a single wing
Liang and Dong [55]	3D computational (forward flight)	Significant vortex interactions occur between the fore and hind wing during flight
Lai and Shen [56]	Experimental (hovering)	At a phase angle of approximately 180°, the LEV produced by the hind wing is significantly reduced compared to the LEV of a single wing

production in both hovering and forward flight, vortex and wing interactions, and effect of wing spacing.

1.3.1. Phase angle and force production in hovering motion

The correlation between the phase angle and flight mode in dragonflies has led to a number of studies concerning the relationship between the phase angle and the force production of tandem flapping wing configurations, both experimentally and computationally. Most studies focused on tandem wings in hovering motion [32–38]. Results by Wang and Russell [35] and Lan and Sun [37] both showed that the maximum resultant force was produced when the wings flap inphase, while Wang and Russell also showed that the highest efficiency was achieved when the wings flapped with a phase angle near 180°. Usherwood and Lehmann experimentally demonstrated that certain phase angles increased the efficiency of the tandem wing, but in their case, maximum efficiency was achieved when $\psi=90^\circ$ [32]. They concluded that this increase in efficiency was due to the hind-wing extracting energy from the wake of the fore-wing by removing swirl. Meanwhile, most of these studies showed that the lift of both the fore and hind wings was noticeably reduced from that of a single wing at most phase angles [32,33,36,37].

1.3.2. Phase angle and force production in forward flight

The relationship between force production and the phase angle has also been studied for tandem wings in forward flight experimentally [39–42] and numerically [43–45]. Studies by both Akhtar et al. [43] and Warkentin and DeLaurier [39] showed that for certain phase angles, the propulsive efficiency of the tandem wing arrangement was almost double that of a single wing. This mirrors the results mentioned earlier by Schmidt [24], Bosch [25] and Tuncer and Platzer [26]. Both Huang and Sun [44] and Wang and Sun [45] simulated 3D tandem wings at different phase angles and advance ratios, using a Navier–Stokes solver. Huang and Sun found that at all advance ratios, the lift and thrust coefficients of the tandem wing case were nearly constant and equal to a single wing when the hind-wing led the fore-wing, but when the fore-wing led the hind-wing, they found that the lift and thrust coefficients were noticeably reduced [44]. Wang and Sun, however, demonstrated that the resultant force coefficient of the tandem configuration was noticeably lower than a single wing at most of the tested phase angles at all advance ratios [45]. At each advance ratio, however; the resultant force coefficient nearly equaled that of a single wing at one of the tested phase angles, which increased from 0° to 90° as the advance ratio increased.

1.3.3. Vortex and wing interaction

The dynamic by which the phase angle affects force production is often associated with variations in the wing–vortex interactions between the fore and hind wings. Work by Saharon and Luttgess with a robotic tandem wing configuration showed that adjustments in the phase angle caused variations in the vortex interactions between the fore and hind wings [40–42]. While they did not measure force data, they hypothesized that the variations in the vortex interactions could influence force generation. Such variation in the vortex interactions has been linked to changes in the force production by other sources [33,43,46]. Variation in force generation due to vortex interactions with the hind-wing would suggest that other parameters could affect force generation similarly to changes in the phase angle. Changes in the wing spacing and advance ratio could both potentially alter the point in the flapping cycle that the hind-wing interacts with vortices shed from the fore-wing and affect the force generation. Wang and Sun [45] showed that the phase angle at which the resultant force peaked changed as the advance ratio was increased while

Maybury and Lehmann [33] saw that the phase angle at which peak lift production occurred changed as the fore and hind wings were moved closer together; though neither of the two studies attempted to link these changes in the force production specifically to altered vortex interactions. Broering et al. [46] linked the variation in force production of the hind-wing to different vortex interactions between the fore and hind wings that altered the LEV generated by the hind-wing at different phase angles. It was also observed by Rival et al. [47] that certain vortex interaction not only increased thrust but also allowed the hind-wing to extract energy from the fore-wing. Rival et al. [48] experimentally studied a nominal two-dimensional tandem configuration. They found that only the tandem phasing of 90° could generate similar levels of thrust when compared to the single wing. Furthermore they found that force and vortex development on the fore-wing was unaffected by the tandem configuration.

1.3.4. Effect of wing spacing

Lim and Tay [49] simulated a tandem configuration in forward flight and different phase angles as well as different spacings between the fore and hind wings. They demonstrated that at an optimum spacing and phase angle, the tandem wing has better performance than the single wing. They also described how variations in vortex interactions between the two wings affected the force coefficients and efficiencies [49]. Broering and Lian [50] investigated the impacts of phase angle and wing spacing on the tandem wing aerodynamics. Kumar and Hu [51] experimentally showed that in tandem configuration the wake structures is affected by the wing spacing. They demonstrated that the wings acted as a single wing when they were too close and acted as two separated wings when they were far from each other. Finally, tandem wings have also been tested for MAV applications. Among them, Jones et al. [52] and Platzer et al. [9] designed and tested fixed tandem wing MAVs, Zhang [53] studied the unsteady aerodynamics of a morphing tandem wing UAV, and English et al. experimentally [54] tested the performance of a tandem wing MAV.

Table 1 shows a summary of studies that have analyzed the phase relationship between tandem flapping wings.

1.4. Wind gust and flapping wings

Due to their low inertia and low flight speeds, MAVs are very sensitive to wind gusts which have comparable speed as the MAVs and can severely affect the vehicle stability [10]. The problem can be further complicated by the variation in the layout of urban environments. In urban environments the wind profiles can differ greatly from area to area. The chaotic behavior of the local incoming wind and the behavior of moving objects within the immediate area further complicate the problem. In wind tunnel tests carried out by Carpenter and Locke [57] it was shown that terrain factors such as the size of, the spacing between, the general smoothness of, and the number of non-homogenous terrain elements all play a role in the gust amplitude. Experimental measurements by Dutt [58] demonstrated the large influence of building geometry and spacing on the amplification of wind speeds. He noted that the alleyways between buildings had significant channeling effects that lead to large increases in the local wind velocity. Kastner-Klein et al. [59] and Vachon et al. [60] experimentally showed that turbulence created by traffic is a significant source of disturbance when compared to the mean wind flow. This turbulence is attributed to both the increases in the thermal energy from the traffic and the kinetic energy imparted by the traffic motion. It is no surprise that Rizzetta and Visbal [61] pointed out that maneuverability/gust tolerance is one

of the two broad categories for the engineering requirements of MAVs (the other category is range/endurance).

There have been limited studies to understand the impact of wind gust on MAV performance. Among them, Lian and Shyy [62] numerically studied the influence of wind gust on fixed wing MAVs. In their study the wind gust was modeled as a single frequency harmonic flow. They showed that the oscillations in the flow velocity can prompt flow to transition from laminar into turbulence. Additionally they showed that the response of a flexible wing in oscillatory flow is similar to that of a rigid airfoil. In another paper Lian and Shyy [3] showed that a flapping wing can alleviate the force variations due to gust. Kerstens et al. [63] studied the effects of gusting on a fixed semi-circular wing. Their studies looked at the phase between the lift variation and the oscillating freestream, noting that the phase is dependent on both the angle of attack and the dimensionless frequency k ($\pi f c/u_{ave}$). They proposed a gust suppression active control strategy that used pulsed blowing jets to modify the flow around an airfoil. They showed that the strategy could reduce the variation in the force generation but it added higher frequency oscillations from the control mechanism. Golubev et al. [64] and Lap et al. [65] performed numerical analysis on the interactions between wind gusts and airfoil flight response wherein the wind gusts were represented by a Taylor-like vortex. They showed correlations between the strength and size of the vortex and the fluctuation in the lift generation. They found that large force fluctuations occurred at the high angles of attack. Additionally they studied the impact of wind gusts on a flapping airfoil and observed that the flapping motion could decrease the response in the lift force. Prater and Lian [66] studied the response of a stationary airfoil in gusty environment using an analytical approach and a computational fluid dynamics approach. They found that the analytical approach tended to predict a lower lift variation than the CFD approach. The under-predicted amount increased with the angle of attack and oscillation frequency. The under-prediction by the analytical approach is due to the fact that at high angles of attack and high frequencies the flow is no longer attached hence it violates the attached flow assumption of the analytical approach. Later they extended the previous wind gust study from stationary airfoils to flapping airfoils and from a single airfoil to multiple airfoils [66]. They studied the impact of wind gust on the aerodynamic performance of flapping airfoils. Comparisons were made with a stationary airfoil to illustrate the benefits of flapping airfoils in gust resistance. Different tandem configurations were explored to understand the gust impact on tandem wings.

1.5. Corrugated wings

Due to MAV's slow flight speed, the chord Reynolds number across the wing is low, 10^2 – 10^4 . At such a low Reynolds number, the flow across the wing is typically laminar. As shown in Fig. 2 the performance of conventional smooth airfoils deteriorates once the Reynolds number drops below 10^5 . The lift-to-drag ratio is the measurement of the effectiveness of an airfoil which is proportional to the gliding ratio and climbing ability of the airfoil [67]. Laminar flow separation typically leads to premature stall and dramatic decrease in the lift and increase in the drag [62,67]. To mediate the effects of stalling conditions and the resulting poor lift-to-drag ratio at low Reynolds number region, new airfoil designs must be created.

Corrugated wings used by dragonflies have been proposed in recent years for low Reynolds number flow conditions. Observations of dragonfly flight seem to indicate that corrugated wings are suitable for low speed flight. Examining an *Aeshna cyanea*'s forewing reveals a highly corrugated structure where the corrugation varies spanwise and chordwise along the wing. The corrugation

provides stiffening of the wing while allowing torsion to occur. Because of the dragonfly's unusual wing structure, it does not resemble any traditional airfoils; it was originally assumed that such a wing performs poorly in flight with low lift and high drag due to this unusual structure. However, several studies have led to multiple conclusions about the use of corrugated structures 1–4.

Two early wind tunnel experiments conducted on corrugated wings by Rees [68] and Rudolph [69] concluded that the corrugation provides no aerodynamic benefits. However they both suggested that fluid flowing over the corrugation could become trapped inside the folds. This trapped fluid would either rotate slowly or remain stagnant. Rudolph also noted that the only benefit a corrugated wing would have over a smooth airfoil is that the corrugation would delay flow separation at higher angles of attack.

Kesel [70] extracted three profiles from the fore-wing of an *A. cyanea*. Each profile was taken from different wing span distances. The aerodynamic performance was measured at a chord Reynolds number of 7880 or 10,000 depending on the profile used. Kesel noticed vortices that formed in the wing's corrugation effectively changed the wing shape and made the corrugated wings behave more like a streamlined wing. It was found the profiles acted similar to asymmetrical smooth profiles or a flat plate. Kesel concluded that an increase in lift generation cannot be obtained from the vortex system from random or uniform corrugations but finely tuned corrugations through evolution.

Murphy and Hu [71] studied the aerodynamic characteristics of a corrugated airfoil, taken from an *A. cyanea*, and compared it with a streamlined airfoil and a flat plate at chord Reynolds numbers of 58,000 and 125,000. The aerodynamic forces measured showed that the corrugated airfoil could generate higher lift, and delay flow separation at higher angles of attack compared to the streamlined airfoil and flat plate. Using a wind tunnel equipped with a Particle Image Velocimetry, they were able to capture images of vortex structures that form inside the valleys of the corrugation. It was determined that the peaks of the corrugation promoted the flow transition from laminar to turbulent, and unsteady vortexes would be captured in the valleys. These vortexes would pull the boundary layer to the surface, keeping the flow attached. This allows the turbulent flow to stay attached through more severe pressure gradients.

Vargas et al. [72] numerically studied a corrugated wing section and further compared to a streamlined profiled version of the corrugated wing section and a flat plate at Reynolds numbers of 500 through 10,000. The flat plate was found to perform best at low Reynolds numbers of less than 5000. Increasing the Reynolds number to 10,000, it was found the corrugated wing section performed better. Vargas et al. concluded that the corrugated wing section preformed best at low angles of attack. At these angles, the wing section experienced increases in pressure drag, but had a reduction in viscous drag due to the existence of recirculation zones inside the corrugations, leading to a negative shear stress contribution.

Recently Kim et al. [73] preformed a numerical study on the corrugated wing section but with Reynolds numbers of 150, 1400, and 10,000 and angles varying from 0° to 40° . The study primarily focused on the effects of the corrugation on lift. Kim concluded that the lift was not directly influenced by the Reynolds number and the corrugation increased the lift through all the angles tested.

Sunada et al. [74] performed water tunnel tests to study the characteristics of 20 wings with the same aspect ratio of 7.25. They found that a 5% camber wing with sharp leading edge produces a better hydrodynamic performance. They also noticed that wing corrugation could also improve the aerodynamic performance. Corrugation was found to be effective because it could increase rigidity. The corrugation makes the thinner wing stronger against

bending and torsional moments so the wing can maintain its profile.

Kesel et al. [75] also demonstrated the structure benefits of a corrugated wing through a finite element analysis. They found that the wing was stabilized primarily by 3-dimensional corrugations. These corrugations dramatically reduced wing deflection by a factor of 20 and reduced stress by 95% compared to a flatter 2-dimensional wing. Kesel concluded that greater structural stability can be achieved through a corrugated profile while using minimum materials, thus creating light, strong wings.

The majority of studies carried out have been with scale models of dragonfly wing sections from the *A. cyanea*'s fore-wing at high Reynolds numbers beyond 10^4 . The study of corrugated wing at the low Reynolds number region was recently conducted by Hord and Lian [76]. They investigated a corrugated airfoil taken from an *A. cyanea* dragonfly at the Reynolds number of 1000. To further understand its structural implication, a static finite element analysis was also performed to understand wing deflection under uniform loading.

2. Numerical methods

The tandem and corrugated wing aerodynamics can be described by the unsteady incompressible Navier–Stokes equations. Written in primitive-variables these equations are as follows:

$$\mathbf{u}_t + (\mathbf{u} \cdot \nabla) \mathbf{u} + \nabla p = \nu \Delta \mathbf{u} \quad (3)$$

$$\nabla \cdot \mathbf{u} = 0 \quad (4)$$

where \mathbf{u} is the flow velocity, p is the pressure, ν is the kinematic viscosity and Δ represents the Poisson operator. To avoid the checker-board instability problem associated with the direct discretization of the pressure term, the above equations can be reformulated in the following so called “velocity–pressure” formulation [77]:

$$\mathbf{u}_t + (\mathbf{u} \cdot \nabla) \mathbf{u} + \nabla p - \nu \Delta \mathbf{u} = 0 \quad (5)$$

$$\Delta p - (\nabla \mathbf{u} \cdot \mathbf{u}_x + \nabla v \cdot \mathbf{u}_y + \nabla w \cdot \mathbf{u}_z) - C_d(v) \nabla \cdot \mathbf{u} = 0 \quad (6)$$

The new formulation can be solved using the split-step approach which decouples the solution of the velocity variables from the solution of the pressure. In the velocity–pressure formulation the term $C_d(v) \nabla \cdot \mathbf{u}$ is added to damp the divergence. Broering et al. [46] carried out spatial discretization over composite overset grids using a second order accurate central difference scheme. In their work time integration was carried out using the Adams–Bashforth–Moulton predictor–corrector method. For the predictor step they used a semi-implicit scheme which discretizes the viscous terms using the Crank–Nicolson treatment and the convection terms using the Adam–Bashforth predictor–corrector. The predictor step is

$$\frac{\mathbf{u}^p - \mathbf{u}^n}{\Delta t} = \frac{3}{2} f_E^n - \frac{1}{2} f_E^{n-1} + \alpha A \mathbf{u}^p + (1 - \alpha) A \mathbf{u}^n \quad (7)$$

and the corrector step is

$$\frac{\mathbf{u}^c - \mathbf{u}^n}{\Delta t} = \frac{1}{2} f_E^n - \frac{1}{2} f_E^{n-1} + \alpha A \mathbf{u}^c + (1 - \alpha) A \mathbf{u}^n \quad (8)$$

where superscripts p and c represent the predicted and corrected values, respectively. When α is 0.5 the above method becomes the second order Crank–Nicolson method. An iterative solver, PETSc, can be used to solve the discretized system of equations [78].

At the Reynolds numbers of 5000 and less Broering et al. [46] assumed flow is laminar. While a Reynolds number of 5000 is too high to be considered purely laminar, several studies show only

small differences in the force histories when using a laminar model compared to a turbulent model at Reynolds numbers below 60,000 [79–82].

An overlapping moving grid method is adopted [83] to handle the wing motion. This method enables the use of boundary-conforming structured grids in order to achieve high quality representation of the boundaries associated with the airfoil surface while still allowing the use of Cartesian grids to represent the flow field so that the efficiencies inherent to such grids can be exploited. In the overlapping grid method, interpolation points are located in the overlapping region between different grids and are used to couple the solutions. As the body moves, the grid associated with the body moves with it, meaning that only the interpolation points between overlapping grids must be recalculated as opposed to the need to regenerate the whole mesh.

Fig. 5 shows a schematic of the overlapping grid used for tandem wing analysis. An O-type grid is generated around the airfoil using a hyperbolic grid generation technique. A high resolution wake grid is used to capture the wake structures between the airfoils. The fine wake grid and background grids are all of uniform density. The airfoils have the smallest grid spacing, with each subsequent grid having increasing grid spacing up to the coarse background grid which has the largest grid spacing. The entire domain is 20 chord lengths in the x and y directions with the tandem configuration centered in the domain. For the inlet boundary on the left the Dirichlet boundary condition is assigned while on the right side, as well as the top and bottom, a zero gauge pressure outlet condition is used.

To establish the validity of the code for the numerical simulation of flapping wing problems, Broering et al. [46] studied a dynamic stall case and compared with both experimental and numerical results [84–86].

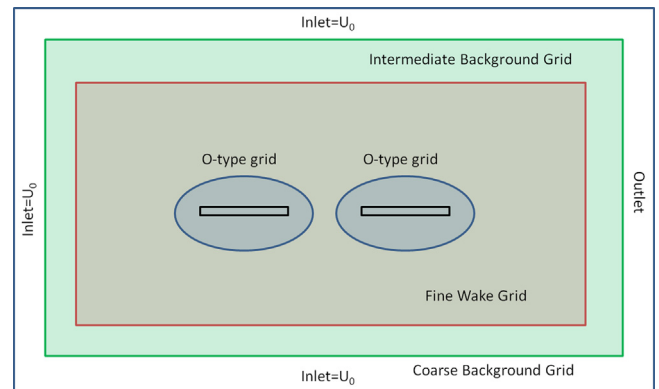


Fig. 5. Schematic of the computational grid and boundary conditions used in the study (not shown to scale) [46].

Table 2
Values used for the different parameters in the kinematic equations.

Parameter	Single/Fore	Hind
α_0	20°	20°
F (Hz)	0.3	0.3
ϕ_a (deg)	90	90
a_{ave} (deg)	5	5
h_0	0.5c	0.5c
ϕ_h (deg)	0°	0°, 90°, 180°
St	0.3	0.3
k	0.942	0.942

3. Tandem wing aerodynamics

3.1. Effect of phase angle

Broering et al. [46] investigated the effect of phase angle on the tandem wing aerodynamics. The flapping kinematics used in their study was a combination of sinusoidal pitching and plunging, with the pitch axis at $0.25c$ from the leading edge. Their intent was not to exactly replicate dragonfly kinematics, which can vary widely depending on the flight mode and trajectory [87], but rather to study a tandem configuration undergoing simple periodic motion to reveal the pertinent wing/vortex and vortex/vortex interaction features. The flapping kinematics used are

$$\alpha(t) = \alpha_0 \cos(2\pi ft + \phi_\alpha + \phi_h) + \alpha_{ave} \quad (9)$$

$$h(t) = h_0 \cos(2\pi ft + \phi_h) \quad (10)$$

where $\alpha(t)$ is the pitching angle, $h(t)$ is the plunging displacement, t is time, f is the flapping frequency, α_0 is the pitching amplitude, h_0 is the plunging amplitude, ϕ_α is the phase for pitch, α_{ave} is the average AoA, and ϕ_h is the phase for plunge. The parameters used for the kinematics for the single, fore and hind wings are shown in Table 2.

The phase angle between pitch and plunge, ϕ_α , was chosen to be 90° (pitch leading plunge) which has been shown to be most

efficient for flapping wings from a number of sources [19,52]. The average angle of attack was set such that a moderate amount of cycle averaged lift was produced. The kinematic parameters used for the single wing were the same as those used for the fore and hind wings.

Both experimental and numerical results from previous studies show mixed results when the force coefficients of tandem wings are compared to a single wing (Tandem outperforms single [39,43], single outperforms tandem [32,36]). Meanwhile, it seems clear that tandem wings can obtain higher efficiency when flapping with the optimal phase angle. In their study, Broering et al. [46] investigated the phase relationship between tandem flapping wings

Table 3
Summary of lift, thrust and resultant for single, fore and hind wings [46].

Wing	Lift	Lift (%)	Thrust	Thrust (%)	Resultant	Resultant (%)
Single	0.807	–	0.350	–	0.879	–
0° Phase fore	0.924	14.5	0.459	31.4	1.032	17.4
90° Phase fore	0.890	10.4	0.433	24.0	0.990	12.6
180° Phase fore	0.941	16.7	0.389	11.3	1.018	15.9
0° Phase hind	0.429	–46.8	0.660	88.8	0.787	–10.5
90° Phase hind	0.398	–50.6	0.070	–79.9	0.404	–54.0
180° Phase hind	0.378	–53.1	0.088	–74.9	0.388	–55.9

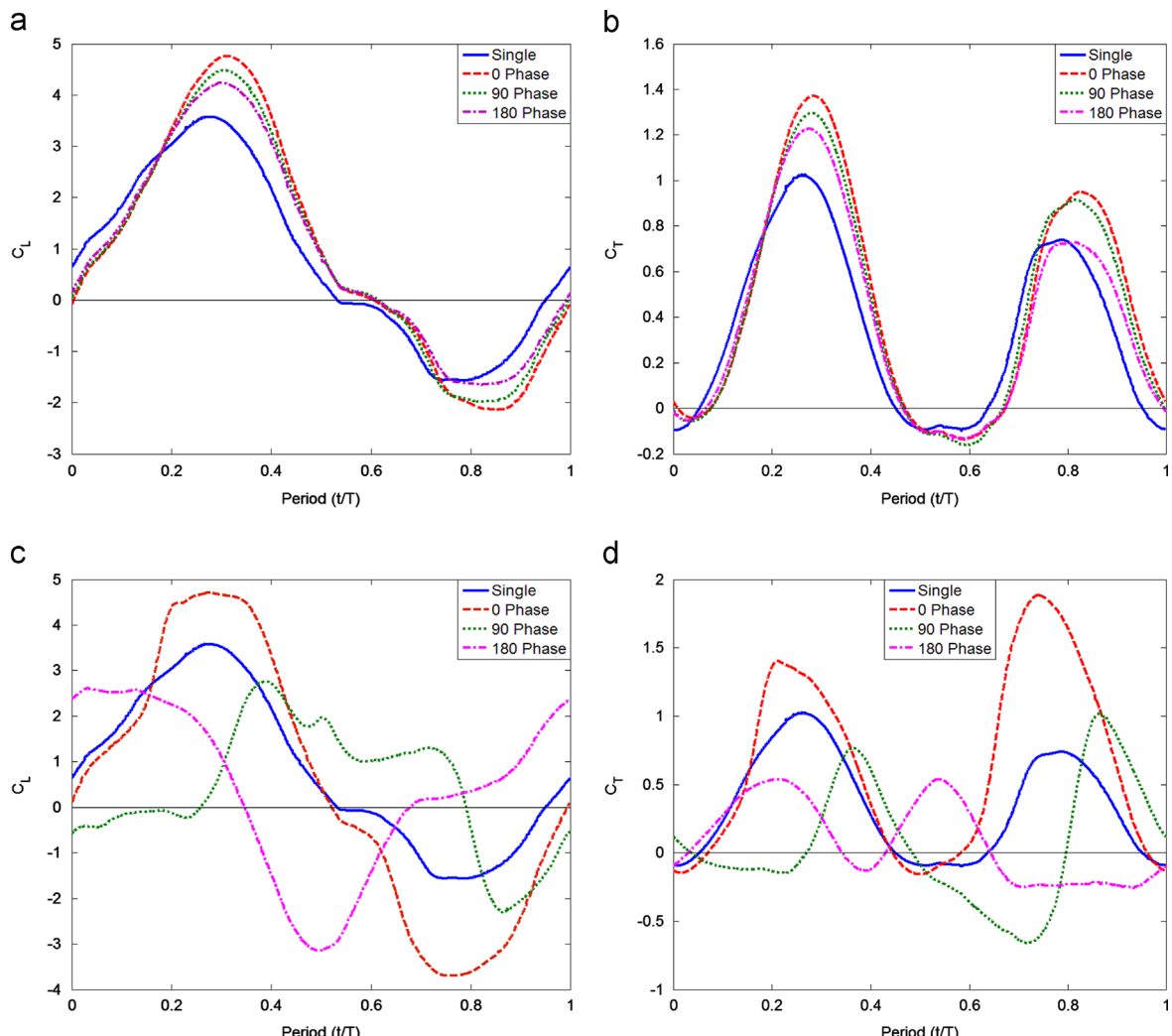


Fig. 6. (a) Lift coefficient during period for single and fore wings. (b) Thrust coefficient during period for single and fore wings. (c) Lift coefficient during period for single and hind wings. (d) Thrust coefficient during period for single and hind wings. [46].

using a 2D model. Three different phase relationships were considered, hind-wing leading fore-wing by 0°, 90°, and 180° (the phase lag was applied to both the pitching and plunging motions together). While three phase angles alone may not be enough to determine optimization [88], it should be enough to demonstrate the broad effects that the phase angle has on the aerodynamics. In all cases they studied the wing spacing was equal to one chord length. Detailed comparisons were made with the case of a single airfoil with the same flow conditions, kinematics, and geometry (including chord length). The tandem and single wing cases were tested at a Strouhal number of 0.3, based on the observations by Taylor et al. that most natural fliers flap in a Strouhal number range of 0.2–0.4 [14]. Results for all cases were taken after periodic motion had been established.

In their work the comparisons between the tandem wing and single wing were made for two purposes. First, to compare the hind-wing performance with and without a fore-wing. Second, to compare the performance of the tandem configuration on a system level (fore and hind wing combined) to the performance of a single wing. Since the flow conditions and flapping kinematics are the same between the tandem and single wings, any differences in the force coefficients are due to the tandem wing interaction. That is, if the two tandem wings were isolated, then the force coefficients would be identical to a single wing, therefore any change from the single wing results must be due to the tandem wing interaction.

3.1.1. Aerodynamic forces

The fore and hind wing results were compared individually to a single wing in order to determine the effect of the fore-wing on the hind-wing (and vice versa). The lift, thrust and resultant coefficients were calculated for each wing individually as

$$C_L = \frac{L}{0.5\rho AU^2} \quad (11)$$

$$C_T = \frac{T}{0.5\rho AU^2} \quad (12)$$

$$C_R = \frac{\sqrt{L^2 + T^2}}{0.5\rho AU^2} \quad (13)$$

where C_L , C_T , and C_R are the lift, thrust and resultant force coefficients, ρ is the fluid density, A is the planform area with unit depth, U is the freestream velocity and L and T are the lift and thrust forces. Fig. 6 shows the transient lift and thrust coefficients, over a single flapping cycle, for both the fore and hind wings at all the three tested phase angles, 0°, 90° and 180° (hind-wing leading) as well as the same values for a single wing.

Fig. 6(a) and (b) show that the presence of the hind-wing has a notable effect on the peak lift and thrust coefficients of the fore-wing during the cycle. The increase in the magnitude of these peaks varies with phase angle, with the 0° phase case showing the largest increase. This effect is not surprising given the results of Jones et al. [89] that show that a pair of oscillating airfoils to the rear of a fixed fore-wing can cause an entrainment effect on the fore-wing and increase lift. Other than the increased peaks in lift and thrust, the fore-wing results are fairly similar to a single wing.

The lift and thrust coefficients for the hind-wing, shown in Fig. 6(c) and (d), vary much more wildly from the single wing and for different phase angles than the fore-wing. This is likely due to the change in wing-wing vortex interactions caused by different phase angles. When the tandem wings flap with 0° phase lag, the hind-wing experiences large increases in the peak lift and thrust coefficients with no noticeable phase lag. Flapping with 90° and 180° phase lag; however, causes the hind-wing to experience noticeable decreases in the peak lift and thrust coefficients, lower

even, than the single wing case. There are also large phase lags in the lift and thrust coefficients of the hind at 90° and 180°. It is important to note that the data in Fig. 6(c) and (d) is normalized so that at any point along the x -axis, all four cases are at the same position in the flapping cycle (origin is at the top of the downstroke). Notably, this causes the hind-wing of the 90° case to produce all of its positive lift at the second half of the downstroke and first half of the upstroke, while the hind-wing of the 180° case produces most of its positive lift during the second half of the upstroke and first half of the downstroke.

Table 3 summarizes the cycle averaged lift, thrust and resultant force coefficients for the single wing and the fore and hind wings of each tandem case. It also shows the corresponding percentage increase or decrease compared to a single wing.

From Table 3 it is clear that the presence of the hind-wing has a positive effect on the force coefficients of the fore-wing. Compared to a single wing, without a hind-wing, the fore-wing shows increases in the average lift, thrust and resultant coefficients. The phase angles tested only show relatively small variations in the lift and resultant coefficients, but large variation in the thrust coefficient, with 0° phase showing the largest increase in the thrust coefficient and 180° phase showing the smallest increase in the thrust coefficient.

The presence of the fore-wing has very mixed results on the hind-wing, when compared to a single wing without a fore-wing. The hind-wing shows a decrease in the lift coefficient of about 50%, regardless of phase angle while the thrust coefficient is increased by about 90% for the 0° phase case and decreases by almost 80% for both the 90° and 180° phase cases. The resultant coefficient of the hind-wing is reduced at all three phase angles, with only a 10% reduction at 0° and just over a 50% reduction at 90° and 180°.

Table 4 compares the power coefficient as well as the propulsive, lift and resultant efficiencies at each phase angle. The propulsive, lift and resultant efficiencies are calculated using

$$\eta_P = \frac{C_T}{C_P} \quad (14)$$

$$\eta_L = \frac{C_L}{C_P} \quad (15)$$

$$\eta_R = \frac{C_R}{C_P} \quad (16)$$

Table 4

Power coefficient and lift, propulsive and resultant efficiencies for the single wing and the fore and hind wing at each phase angle [46].

Wing	C_P	η_P (%)	η_L (%)	η_R (%)
Single	1.137	30.8	71.0	77.3
0° Phase fore	1.500	30.6	61.6	68.8
90° Phase fore	1.422	30.5	62.6	69.6
180° Phase fore	1.268	30.7	74.2	80.3
0° Phase hind	1.920	34.4	22.3	41.0
90° Phase hind	0.410	17.1	97.1	98.5
180° Phase hind	0.488	18.0	77.5	79.5

Table 5

Comparison of lift, thrust and resultant for two isolated single wings to each tandem configuration [46].

Wing	Lift	Lift (%)	Thrust	Thrust (%)	Resultant	Resultant (%)
Single	0.807	–	0.350	–	0.879	–
0° Phase	0.677	–16.1	0.560	60.1	0.878	–0.11
90° Phase	0.644	–20.1	0.252	–28.0	0.691	–21.3
180° Phase	0.660	–18.2	0.239	–31.8	0.701	–20.2

where η_P is the propulsive efficiency, C_T is the thrust coefficient, η_L is the lift efficiency, C_L is the lift coefficient, η_R is the resultant efficiency and C_R is the resultant coefficient. The power coefficient C_P is calculated using

$$C_P = \frac{1}{0.5\rho AU^3} \int_0^T [-(\mathbf{L} \cdot \mathbf{V}) - (\mathbf{M} \cdot \boldsymbol{\omega})] dt \quad (17)$$

Table 6

Power coefficient and lift, propulsive and resultant efficiencies for the single wing and the tandem configuration at each phase angle [46].

Configuration	C_P	η_P (%)	η_L (%)	η_R (%)
Single	1.137	30.8	71.0	77.3
0° Phase	1.710	32.7	39.6	51.3
90° Phase	0.916	27.5	70.3	75.5
180° Phase	0.878	27.2	75.1	79.9

where ρ is the fluid density, A is the planform area with unit depth of an individual wing, U is the flow velocity, T is the flapping period, \mathbf{L} is the instantaneous lift force, \mathbf{V} is the instantaneous wing vertical velocity, \mathbf{M} is the instantaneous pitching moment, and $\boldsymbol{\omega}$ is the instantaneous rotational velocity.

The results in Table 4 are quite interesting. First, when operating at a 90° and 180° phase lag, the hind-wing requires very little power for actuation. Despite undergoing the exact same flapping kinematics, the hind-wing only requires 36% and 43% of the power needed to actuate the single wing, when operating at 90° and 180° phase angles, respectively. This clearly shows that the hind-wing is able to extract power from the wake of the fore-wing at certain phase angles. The large decrease in the actuation power was a result of the phase shift in the lift shown in Fig. 6c. Both the 90° and 180° phase cases produce a large amount of positive lift during the upstroke, which corresponds to the direction of motion of the wing and reduces the power needed for actuation.

The hind-wing has no noticeable effect on the propulsive efficiency of the fore-wing, regardless of phase angle. Its effect

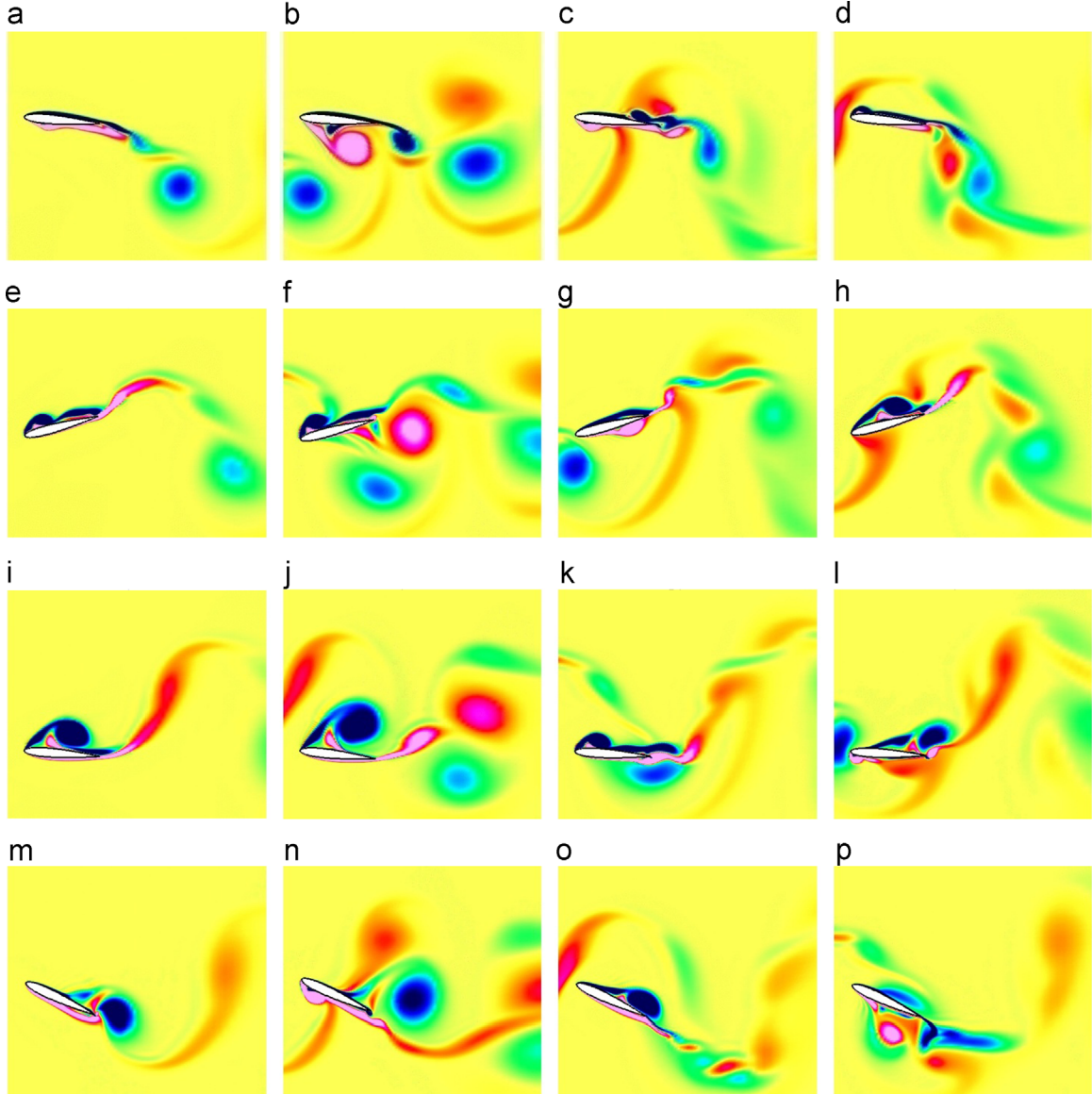


Fig. 7. Different phase angles change the vortex shedding between the fore and hind wing, which affects the vorticity around the hind-wing. The first row shows the four different cases at 0% flapping cycle (a–d), the second row – 25% (e–h), the third row – 50% (i–l) and the fourth row – 75% (m–p). The first column is the single wing, the second column is the 0° hind-wing, the third column is the 90° hind-wing and the fourth column is the 180° hind-wing [46]. (For interpretation of the references to color in this figure legend, the reader is referred to the web version of this article.)

on the fore-wing's lift efficiency is more noticeable, decreasing it by about 12% at phase angles of 0° and 90° and increasing it slightly at 180°. For the resultant efficiency, the fore-wing for the 0° and 90° cases showed about a 12% drop in efficiency, compared to the single wing, while the fore-wing for the 180° case showed a slight increase in the resultant efficiency.

The effect of the fore-wing on the hind-wing shows mixed results for efficiency. At 0° phase, the hind-wing showed a small increase in propulsive efficiency over a single wing, but at 90° and 180° it only had about half the propulsive efficiency of a single wing. Conversely, the hind-wing flapping at 0° phase lag only had approximately one-third the lift efficiency of the single wing, while the 90° and 180° hind-wings showed an increase in the lift efficiency of 37% and 9% respectively. The resultant efficiency of the hind-wing at 0° phase lag was about half of the resultant efficiency of a single wing while the 90° phase hind-wing showed an increase of 30% and the 180° phase hind-wing showed a slight increase in the resultant efficiency.

The performance of the tandem configuration on a systems level (combined fore and hind wing) to a single wing ([Table 5](#)). The lift thrust and resultant coefficients are calculated using

$$C_L = \frac{L_F + L_H}{0.5\rho(A_F + A_H)U^2} \quad (18)$$

$$C_R = \frac{\sqrt{(L_F + L_H)^2 + (T_F + T_H)^2}}{0.5\rho(A_F + A_H)U^2} \quad (19)$$

$$C_T = \frac{T_F + T_H}{0.5\rho(A_F + A_H)U^2} \quad (20)$$

where L_F and L_H are the lift of the fore and hind wing, T_F and T_H are the thrust of the fore and hind wing, and A_F and A_H are the planform area of the fore and hind wing with unit depth. Since the combined force production of the tandem configuration is normalized by the

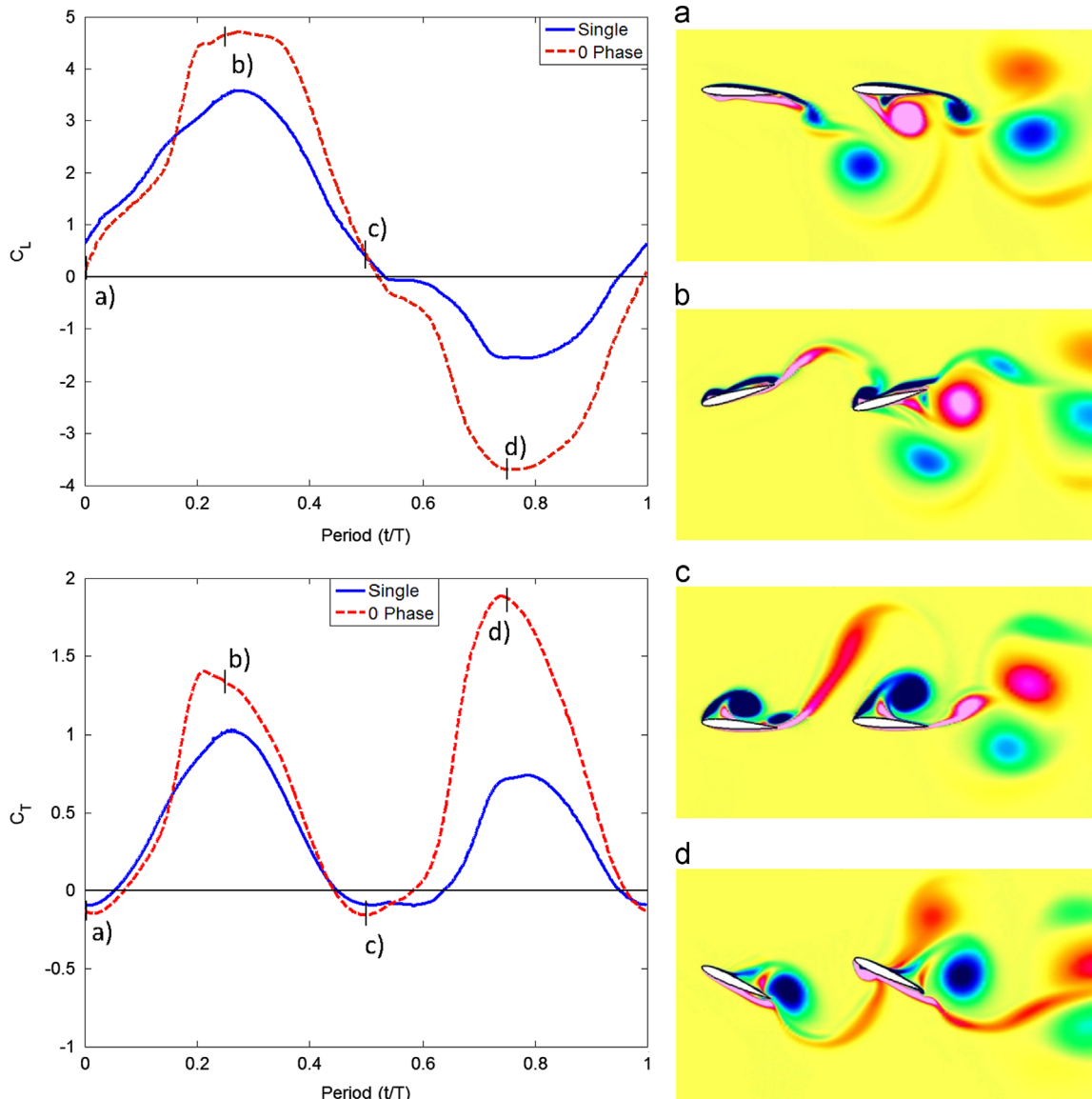


Fig. 8. Lift and thrust coefficients plotted vs. time and vorticity contours at 0%, 25%, 50% and 75% flapping cycle for the tandem wing flapping with 0° phase lag. Constructive vortex interactions increase the size of the LEVs generated by the hind-wing which increases the peak lift and thrust production [46]. (a) $t/T = 0$, (b) $t/T = 0.25$, (c) $t/T = 0.5$ and (d) $t/T = 0.75$.

planform area of both wings, the lift, thrust and resultant coefficients can be compared to the same results for a single wing.

Table 5 shows the results for cycle average lift, thrust and resultant coefficients for each tandem configuration (fore and hind wings combined) compared to the results of a single wing.

The data from **Table 5** shows that the magnitude of the resultant for the 0° phase case is similar to that of the single wing, while both the 90° and 180° phase cases exhibit about the same decrease in the resultant, about 20%. The total lift and thrust of the 90° and 180° phase case is less than the case of the single wing. The 0° phase case generates 16% less total lift than the single wing, but 60% more total thrust. Overall, the 90° and 180° phase cases are detrimental in terms of lift, thrust and the resultant compared to the single wing. The 0° phase case causes no change to the magnitude of the resultant; however, it inclines the resultant forward, producing more thrust at the expense of lift. **Table 6** shows the power coefficient and propulsive, lift and resultant efficiencies of the tandem wing configuration (fore and hind wing combined) compared to a single wing.

The 0° phase configuration has the highest power coefficient, significantly higher than the single wing value. Switching to either 90° or 180° phase cuts the power coefficient to approximately 50% of the 0° phase case, well below the power coefficient of the single wing. The 0° phase configuration has a slightly higher propulsive efficiency than the single wing, while both the 90° and 180° phase configurations have a slightly lower propulsive efficiency than a single wing. The 0° phase case, however, has a significantly lower lift and resultant efficiency than a single wing, while the 90° and 180° have very similar lift and resultant efficiencies as a single wing.

Summarizing the effects of the phase angle on the tandem wing configuration, it is clear that by switching the phase angle, the tandem wing is able to change its flight mode. When flapping with 0° phase lag, the tandem wing produces a large amount of thrust with a high propulsive efficiency but requires more power for actuation, which lowers the lift and resultant efficiencies. Switching to 90° or 180° phase lags lowers the required power for actuation by 50% and raises the lift and resultant efficiency, but

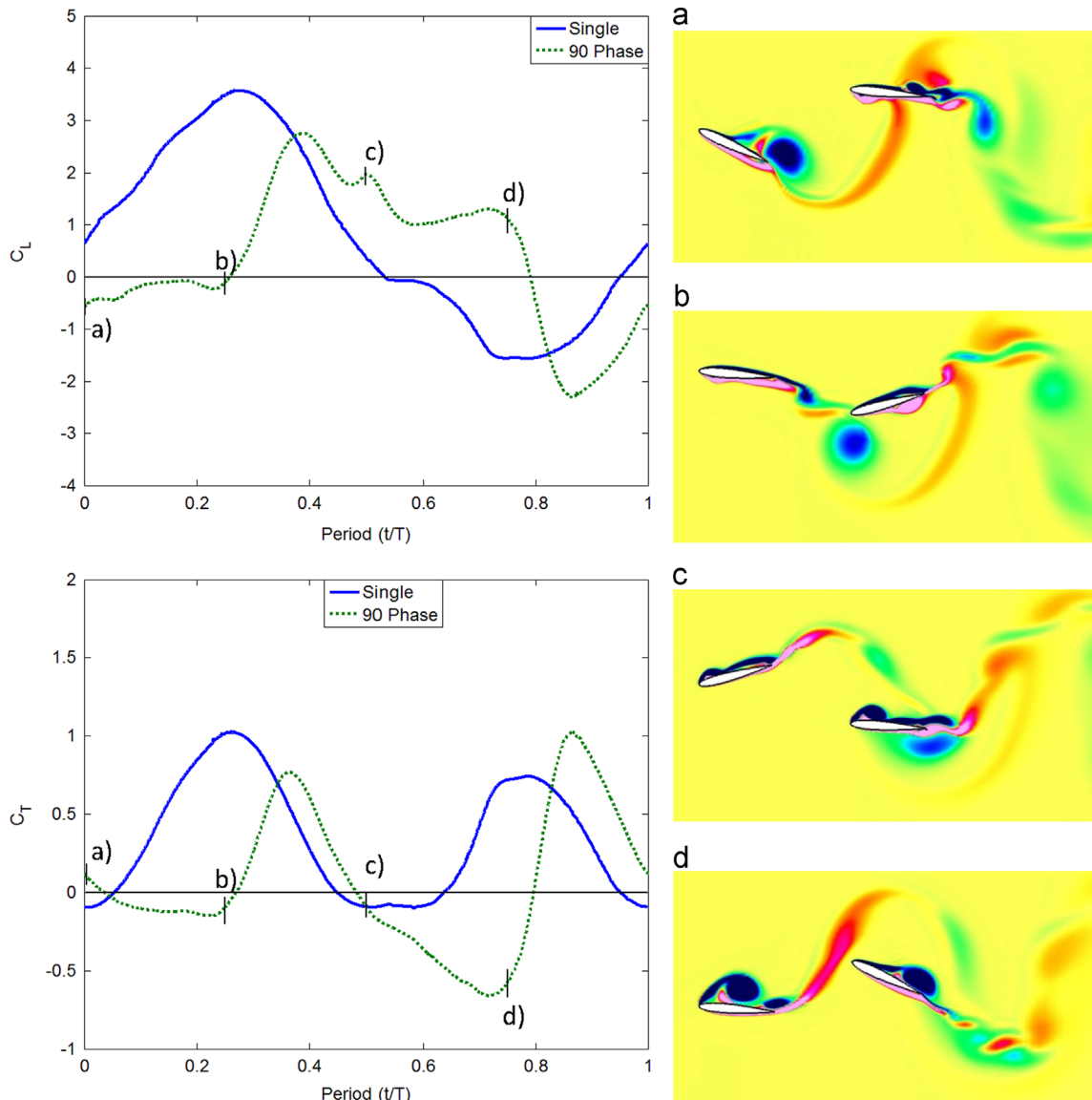


Fig. 9. Lift and thrust coefficients plotted vs. time and vorticity contours at 0%, 25%, 50% and 75% flapping cycle for the tandem wing flapping with 90° phase lag. Destructive vortex interactions decrease the size of the LEVs generated by the hind-wing and cause a phase shift in the lift such that lift is produced on the upstroke [46]. (a) $t/T=0$, (b) $t/T=0.25$, (c) $t/T=0.5$ and (d) $t/T = 0.75$.

at the expense of thrust and propulsive efficiency. Lift production was nearly identical between the three tested phase angles. These results seem to line up with the observed behavior of dragon flies, where they flap inphase for maneuvers and out of phase for cruising flight.

For the parameters studied in this paper, the tandem wing does not definitively outperform the single wing. While flapping with 0° phase lag results in a larger thrust coefficient and a higher propulsive efficiency than a single wing, there is a noticeable reduction in lift and increase in the power coefficient which results in a large decrease in the lift and resultant efficiencies. Switching to a phase lag of 90° or 180° results in similar lift and resultant efficiencies as a single wing as well as a smaller power coefficient, but the single wing still has the larger lift coefficient as well as a larger thrust coefficient and greater propulsive efficiency.

3.1.2. Flow visualization results

Fig. 7 shows the vorticity contours around the single wing and the hind-wings of the three tandem configurations at four different

points in the flapping cycle (0%, 25%, 50%, 75%). Red represents counterclockwise (CCW) vorticity and blue represents clockwise (CW) vorticity. **Fig. 7** is arranged such that each row shows the four different cases at the same point in the flapping cycle. This is specifically highlights how the change in the phase angle affects the vortex generation of the hind-wing.

Fig. 7 shows that the phase angle has a noticeable effect on the size of the leading edge vortex (LEV) generated by the hind-wing. Comparing the different tandem configurations, the 0° phase hind-wing was characterized by constructive vortex interactions, while the 90° and 180° phase cases were characterized by destructive vortex interactions. The constructive and destructive vortex interactions were experimentally studied by Dong and Liang [55]. In their work a heaving and pitching foil was placed behind an oscillating cylinder. Both the foil and the cylinder move forward at a constant speed. They observed that destructive interactions increase efficiency while constructive interactions decrease efficiency, which is consistent with our observations. Zhu et al. [56] conducted an integrated experimental and numerical study to establish the prominent features of flow around a fish. They found

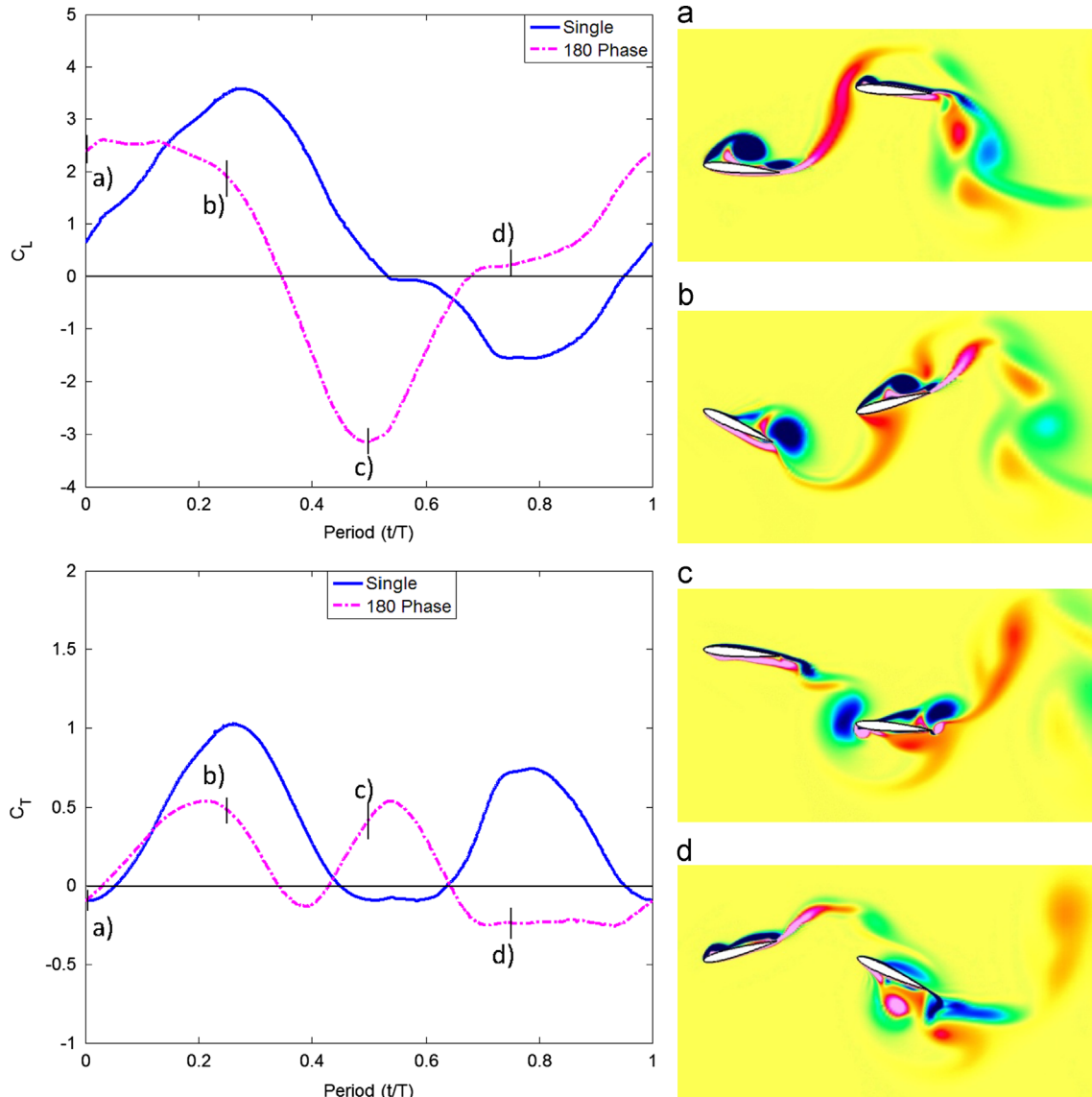


Fig. 10. Lift and thrust coefficients plotted vs. time and vorticity contours at 0%, 25%, 50% and 75% flapping cycle for the tandem wing flapping with 180° phase lag. Destructive vortex interactions decrease the size of the LEVs generated by the hind-wing and cause a shift in the timing of LEV formation [46]. (a) $t/T = 0$, (b) $t/T = 0.25$, (c) $t/T = 0.5$ and (d) $t/T = 0.75$.

that interactions between the body-generated vortices and the tail-generated vorticity affect the propulsive efficiency: a constructive interaction results in high thrust while a destructive one leads to high propulsive efficiency.

For the 0° phase case, constructive interactions with the vortices shed by the fore-wing led to increased size of the LEV's generated around the hind-wing, which is seen clearly in (b), (f), (j), and (n). During the first half of the downstroke (b–f), the

hind-wing passes behind CW vorticity shed by the fore-wing, which interacts with the CW LEV generated on the top of the hind-wing. A similar interaction occurs during the first half of the downstroke (j–n), where the hind-wing passes behind CCW vorticity shed by the fore-wing, which interacts with the CCW LEV generated on the bottom of the hind-wing. This interaction is more noticeable in Fig. 8, which shows the vorticity contours of the fore and hind wing together.

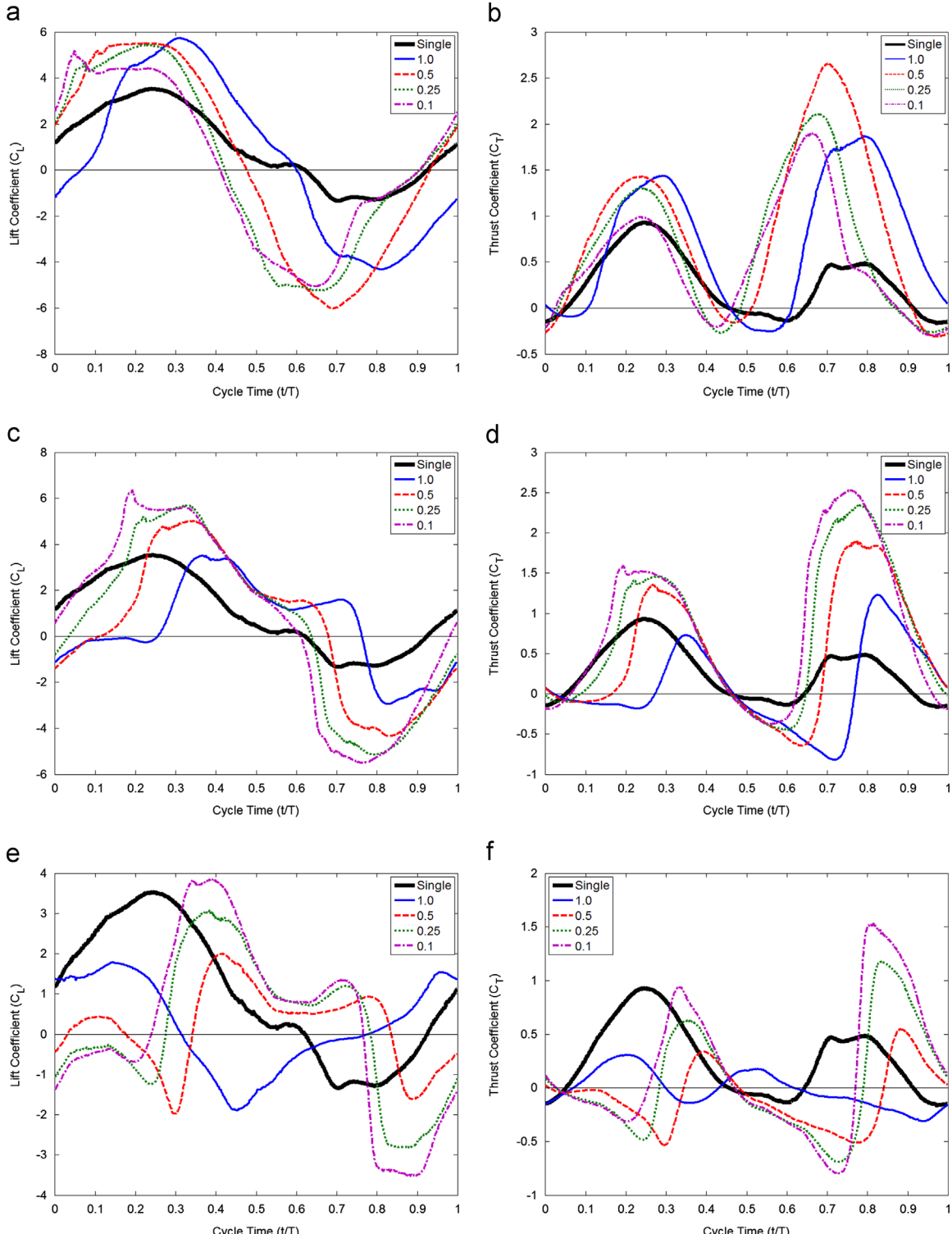


Fig. 11. Transient lift and thrust coefficients for the hind-wing over a single flapping cycle compared to a single wing. Each graph shows the lift or thrust at a single phase angle for the four tested spacings [50]. (a) 0 Phase Lift, (b) 0 Phase Thrust, (c) 90 Phase Lift, (d) 90 Phase Thrust, (e) 180 Phase Lift and (f) 180 Phase Thrust.

For the 90° phase hind-wing, the destructive interaction caused the lack of an LEV on the top of the airfoil during the downstroke, but the generation of an LEV on the top of the airfoil during the upstroke. The first of these destructive interactions occurs as the hind-wing reaches the end of the upstroke and starts on the downstroke (o–c). The hind-wing passes behind CCW vorticity shed by the fore-wing which dampens out the CW LEV that would normally form on the top of the airfoil during the downstroke, while initiating the generation of a CCW LEV on the bottom of the hind-wing. A similar interaction occurs as the hind-wing moves from the end of the downstroke to the beginning of the upstroke (g–k) and passes behind a CW vortex shed by the fore-wing. This creates a CW LEV that stays attached to the top of the hind-wing during part of the upstroke while canceling out the CCW LEV that would normally form on the bottom of the airfoil.

The 180° phase hind-wing experienced similar destructive interactions as the 90° phase hind-wing, but to a lesser extent. At the start of the downstroke (d), the hind-wing has already formed a small CW LEV on top, which is earlier than normal. As it starts on the downstroke (d), the hind-wing passes behind CCW vorticity shed by the fore-wing as the CW LEV is forming on the top of the airfoil. This interaction reduces the size of the LEV formed during the downstroke. As the hind-wing starts its upstroke [1], a CW vortex shed from the fore-wing passes over it. Half of this vortex convects over the top of the hind-wing, while the other half interacts with the CCW LEV forming at the bottom of the airfoil and detaches it from the hind-wing during the upstroke.

Figs. 8–10 compare how the changes in the LEV production of the hind-wing due to different phase angles affects the lift and thrust production of the hind-wing. Each figure depicts results for the 0°, 90° and 180° tandem cases, respectively. The transient lift and thrust coefficients of the hind-wing are plotted to the left along with the single wing as a baseline. Vorticity contours are shown to the right at four different points in the flapping cycle, 0%, 25%, 50% and 75% (the same points as in Fig. 7). These points in the flapping cycle are marked on the lift and thrust graphs as (a)–(d).

Fig. 8 shows the lift and thrust coefficients as well as the vorticity contours for the tandem wing flapping with 0° phase lag. Due to the constructive vortex interaction between the fore and hind wing, the hind-wing generates larger LEVs on both the downstroke and upstroke. During the downstroke, the LEV is generated on the top of the airfoil. With the airfoil pitching downward, the LEV is also on the upstream side of the airfoil. This point corresponds to (b) on the force histories, which is the point of peak lift and thrust production on the downstroke. The same effect is seen on the upstroke. An LEV forms on the bottom of the airfoil, which, with the airfoil pitching upward, is also on the upstream side. This is point (d) on the force histories, and it corresponds to peak lift and thrust production on the upstroke.

Fig. 9 shows the results for the tandem wing flapping with 90° phase lag. Destructive vortex interactions result in the lack of an LEV on the top of the hind-wing during the downstroke. Instead, an LEV is formed on the top of the hind-wing during the upstroke. This corresponds to points (c) and (d) on the force graphs. This causes positive lift to be generated during the upstroke, as well as the large amount of negative thrust, point (d). This negative thrust corresponds with the LEV on top of the airfoil also being oriented on the downstream side of the airfoil, since the airfoil is pitching upward at this point. Because the hind-wing produces a large amount of lift on the upstroke, the power required for actuation is greatly lessened, since the lift production corresponds to the direction of travel of the airfoil.

Fig. 10 shows the results for the tandem wing flapping with 180° phase lag. An LEV forms on the top of the hind-wing during the downstroke, point (a), but its formation is earlier than normal. The LEV is also smaller than normal, and while it forms on the upstream side of the airfoil, it is already convecting away as the pitch angle reaches its maximum point, at (b). At these points, the force histories show decreases in the peak lift and thrust coefficients. From points (c) to (d), a vortex shed from the fore-wing bisects the hind-wing. Half of it convects over the top, downstream facing side of the airfoil, while the other half detaches

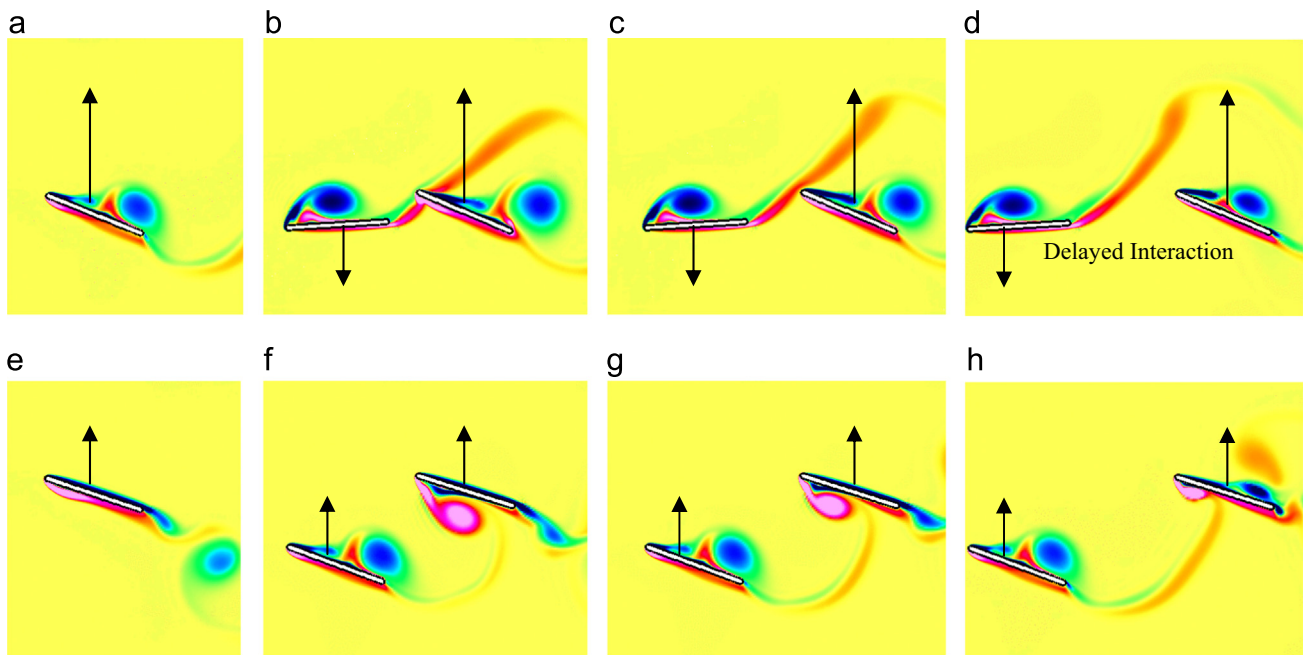


Fig. 12. The vorticity contours of the single wing and the 90° phase angle tandem configuration at different spacings. The large spacing delays and weakens the vortex/wing interaction. The first row shows the single and hind-wing during the upstroke at 68% cycle time while the second row shows the single and hind-wing at 89% cycle time. Arrows indicate the stroke direction [50]. (a) Single, $t/T=68\%$, (b) 0.25c, $t/T=68\%$, (c) 0.5c, $t/T=68\%$, (d) 1.0c, $t/T=68\%$, (e) Single, $t/T=89\%$, (f) 0.25c, $t/T=89\%$, (g) 0.5c, $t/T=89\%$ and (h) 1.0c, $t/T=89\%$.

the LEV from the bottom, upstream facing side. This corresponds to point (d) on the force graphs, where the hind-wing shows positive lift and negative thrust production. This positive lift persists through the last half of the upstroke, due to the earlier than normal LEV formation on the top of the hind-wing, as seen at point (a). Like the 90° hind-wing, the large amount of positive lift produced during the

upstroke is responsible for the large decrease in actuation power necessary for the hind-wing at 180° phase lag.

In summary, Figs. 7–10 show that changing the phase angle changes the vortex interaction between the fore and hind wings. Specifically, different phase angles can be used to change the nature of LEV formation by the hind-wing, which in turn affects

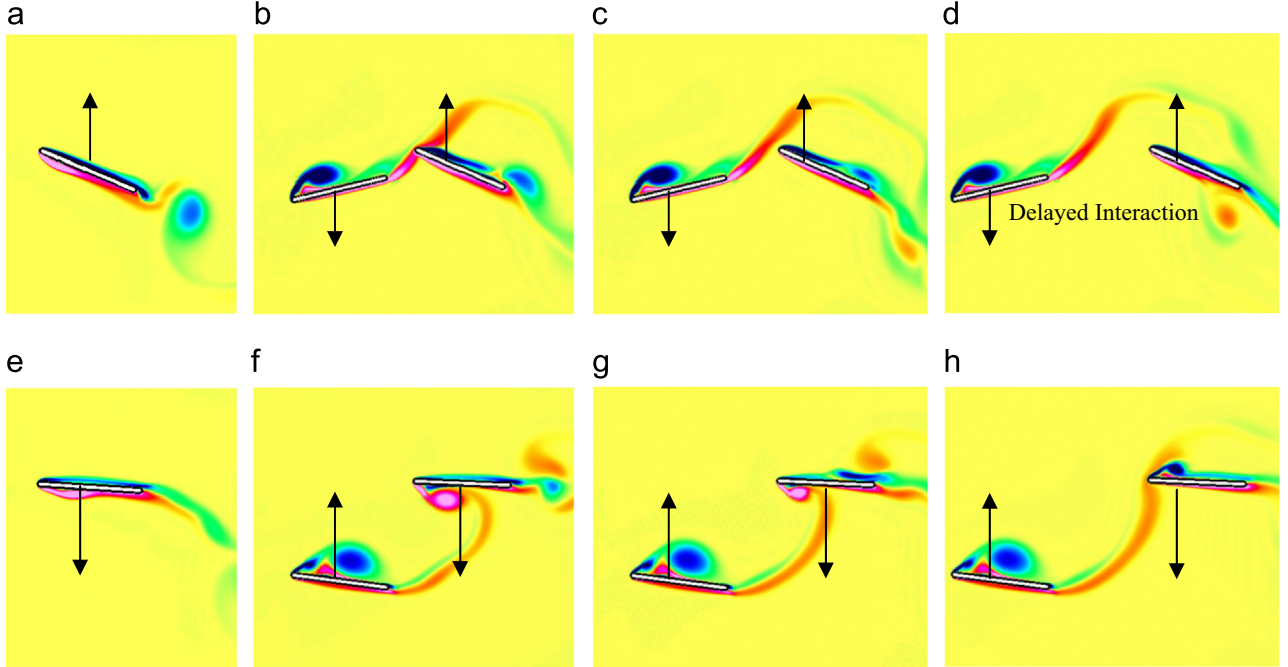


Fig. 13. The vorticity contours of the single wing and the 180° phase angle tandem configuration at different spacings [50]. The vortex/wing interaction is delayed compared to the 90° phase angle tandem configuration case. The first row shows the single and hind-wing during the upstroke at 81% cycle time while the second row shows the single and hind-wing at 2% cycle time. Arrows indicate the stroke direction. (a) Single, $t/T=81\%$, (b) 0.25c, $t/T=81\%$, (c) 0.50c, $t/T=81\%$, (d) 1.0c, $t/T=81\%$, (e) Single, $t/T=2\%$, (f) 0.25c, $t/T=2\%$, (g) 0.5c, $t/T=2\%$ and (h) 1.0c, $t/T=2\%$.

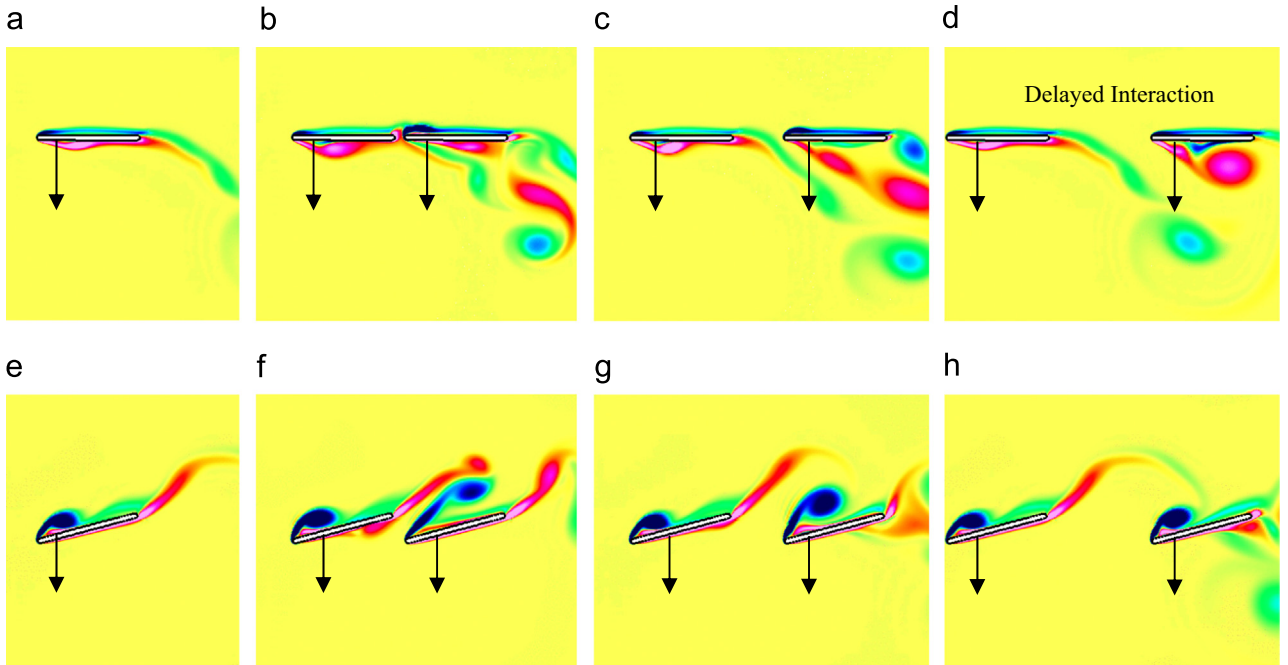


Fig. 14. The vorticity contours of the single wing and the 0° tandem configuration at different spacings [50]. The first row shows the single and hind-wing during the downstroke at 4% cycle time while the second row shows the single and hind-wing at 25% cycle time. Arrows indicate the stroke direction. (a) Single, $t/T=4\%$, (b) 0.1c, $t/T=4\%$, (c) 0.5c, $t/T=4\%$, (d) 1.0c, $t/T=4\%$, (e) Single, $t/T=25\%$, (f) 0.1c, $t/T=25\%$, (g) 0.5c, $t/T=25\%$ and (h) 1.0c, $t/T=25\%$.

the lift and thrust generation of the hind-wing, as shown in Figs. 8–10. When flapping with 0° phase lag, the resulting LEV formation around the hind-wing is similar to a single wing, but the LEV's are larger. This is due to the constructive vortex interactions between the fore and hind wings, where vorticity shed by the fore-wing interacts with like signed LEVs generated by the hind-wing. Due to the larger LEV formation, the peak lift and thrust produced by the hind-wing is increased.

When the hind-wing flaps with 90° or 180° phase lag, the vortex interactions between the fore and hind wings are destructive, where vorticity shed by the fore-wing interacts with opposite signed LEVs generated by the hind-wing. This tends to decrease the size of the LEVs generated by the hind-wing as well as change the timing of LEV formation. For the 90° hind-wing, LEV formation is altered to the point where it forms an LEV on the bottom of the airfoil during the downstroke and on the top of the airfoil during the upstroke. As a result, both the 90° and 180° see phase shifts in lift and thrust generation as well as decreases in peak lift and thrust. As a result of the phase shift in lift production, both the 90° and 180° hind-wings produce a large amount of positive lift on the upstroke, which reduces the power coefficient of both wings.

3.2. Effect of wing spacing

Broering and Lian [50] numerically investigated the impacts of wing spacing on tandem wing aerodynamics. In their study three different phase angles, 0° , 90° , and 180° (hind-wing leading) were simulated at four different wing spacings, $1.0c$, $0.5c$, $0.25c$, $0.1c$. All cases were simulated at a Reynolds number of 5000 based on the shape of a flatplate with 5% chord thickness and rounded edges. The Strouhal number of the flapping wing kinematics is 0.3. In the next we summarize their results.

3.2.1. Aerodynamic force results

Fig. 11 shows the transient lift and thrust coefficients of only the hind-wing over a single flapping cycle at different wing gap spacings for the three tested phase angles, 0° , 90° and 180° (hind-wing leading). The same results for the single wing are also shown to serve as a baseline. In the plots a cycle time, t/T , of 0% is the start of the downstroke and 50% is the start of the upstroke.

The results in Fig. 11 illustrate the significant effect that changing the phase angle or wing spacing can have on the lift and thrust generation of the hind-wing. The effect of the phase angle is considered first. At 0° phase angle, the lift and thrust amplitudes of the hind-wing are much higher than the single wing case at each spacing. When the phase angle is 90° , the hind-wing

has higher force amplitudes than the single wing at the small spacings but not at the large spacing of $1.0c$. Finally, at 180° phase lag, the hind-wing has higher force amplitudes than the single wing through the upstroke but lower force amplitudes during the downstroke for small spacings. At the largest spacing, however, the hind-wing has significantly lower force amplitudes than the single wing.

Next, the impact of the wing spacing is considered. In general, increasing the wing spacing causes a phase lag in both lift and thrust generation. This trend is shown clearly in the case where the fore and hind wings flap with a 90° phase lag. Both the lift and thrust show a clear phase lag in the timing of the lift and thrust generation as the spacing is increased from $0.1c$ to $1.0c$. There is also a trend of increasing lift and thrust amplitudes as the spacing is decreased. The 180° phase case shows nearly the same trend as the 90° phase case. There is a phase lag in both the lift and thrust as the spacing is increased from $0.1c$ to $0.5c$, just as at 90° , but increasing the spacing to $1.0c$ does not show the same trend in the phase lag. The 180° case also exhibits increases in the peak lift and thrust as the spacing is decreased, similar to the 90° case. The trends observed in the 90° and 180° cases are not as evident for the 0° case. While the 0° case exhibits phase lag in the timing of the force generation as the spacing is decreased, it is inconsistent. Also, the peak lift and thrust magnitudes do not show the same increasing trend that is observed with the 90° and 180° cases as the spacing is decreased.

3.2.2. Flow visualization results

The behavior observed in the force data can be explained by analyzing the vorticity contours for each case. Specifically, examining how changes in the phase angle and wing spacing changes the timing of vortex interactions during the flapping cycle of the hind-wing. Figs. 12–14 show the vorticity contours at different spacings for the 90° , 180° and 0° cases, respectively. For the sake of brevity, the vorticity contours are only shown for one half of the cycle (upstroke for the 90° and 180° cases and downstroke for the 0° case) as the upstroke and downstroke exhibit nearly symmetric results.

Fig. 12 illustrates how changes in the wing spacing affect the timing of the vortex/wing and vortex/vortex interactions and how the interactions influence leading edge vortex (LEV) formation during the upstroke of the hind-wing when the wings flap with 90° phase lag. During the upstroke, the hind-wing passes through a vortex shed from the trailing edge of the fore-wing. At the closer spacings this interaction occurs during the first half of the upstroke (68% cycle time). As the spacing is increased, this vortex interaction

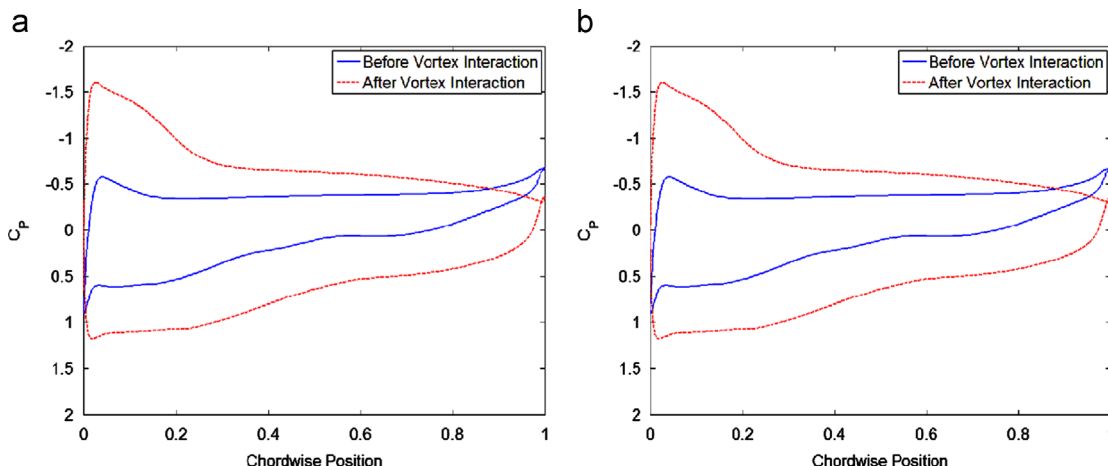


Fig. 15. There is a large increase in suction on the top of the leading edge of the hind-wing that is associated with the passing of the vortex shed by the fore-wing. There is no observable increase for the single wing [50].

is delayed, due to the increased time necessary for the vortex to convect to the hind-wing, and occurs later in the upstroke. This delay in the vortex interaction is clearly observed as a phase lag in the transient lift and thrust data shown in Fig. 11(c) and (d).

The timing of the interaction between the hind-wing and vortex shed from the fore-wing has a noticeable effect on the LEV formation around the hind-wing. The bottom row of Fig. 12 shows the vorticity contours when the hind-wing is at 89% cycle, just before stroke reversal, after the vortex interaction has occurred. The rotation of the shed vortex is the same as the rotation of the LEV that forms on the bottom of the hind-wing (counterclockwise, CCW), which reinforces the LEV generation. At the closer spacings, the vortex interaction is stronger because the vortex shed from the fore-wing has less time to dissipate before interacting with the hind-wing. This results in larger LEV generation by the hind-wing, which corresponds with the increased peak in the transient lift and thrust data as the spacing is decreased. The increased peak in the transient force data can be observed in Fig. 11(c) and (d). On the downstroke, the same interaction and phase lag is observed, except that the vortex shed from the fore-wing and the LEV generated by the hind-wing are clockwise (CW).

Similar to Fig. 12, Fig. 13 shows the vorticity contours at different spacings for the 180° phase case during the upstroke. In this case, the hind-wing passes through the vortex shed by the fore-wing, as in the 90° case, but the vortex interaction occurs significantly later in the upstroke due to a larger phase angle. At the closest spacings, the hind-wing starts to interact with the shed vortex in the second half of the upstroke, at 81% of cycle compared to 68% of cycle for 90° case. As the spacing is increased this interaction is delayed, which corresponds with the phase lag in the force data shown in Fig. 11(e) and (f). This behavior is similar to that observed in the 90° case. At 180° phase lag, however; when the wing spacing is increased to 1.0c, the vortex interaction is delayed until after stroke reversal, which allows the start of LEV formation on top of the hind-wing. The delay is reflected in the force data shown in Fig. 11(e) and (f), in which the 1.0c spacing shows dramatically different pattern from other spacings.

The timing of the vortex interaction has large implications on the LEV generation of the hind-wing. These implications can be observed by comparing the LEVs on the hind-wings in Fig. 13(e)–(h). At the closest spacings, the hind-wing passes through the shed vortex before stroke reversal, which serves to reinforce the LEV formation at the bottom of the hind-wing (both vortices have the same rotation, CCW). As the spacing is increased, the vortex interaction becomes weaker as the vortex shed from the fore-wing has more time to dissipate before interacting with the hind-wing,

resulting in smaller LEV generation. This corresponds with the lower peak lift and thrust observed in the force data as the spacing is increased as observed in Fig. 11(e) and (f). At the spacing of 1.0c, the interaction is delayed until stroke reversal, where the hind-wing starts to form a CW LEV on top. The interaction with the CCW shed vortex dampens out the CW LEV and quickens its shedding, which results in the extremely low lift and thrust production observed for this case in Fig. 11(e) and (f). As with the 90° case, the result on the downstroke are symmetrical to the upstroke except that the rotation of the vortices are reversed.

Fig. 14 shows the vorticity contours at the tested spacings for the 0° phase case during the downstroke. The results are shown for the downstroke rather than the upstroke because the vortex interaction is easier to observe. Similar to the 90° and 180° cases, the hind-wing passes through the vortex shed from the trailing edge of the fore-wing and the interaction is delayed as the spacing is increased. Because the fore and hind wings flap with 0° phase lag, at the smaller spacings, the two wings remain in close proximity to each other throughout the entire cycle. At the 1.0c and 0.5c, the interaction between the CW shed vortex and the hind-wing reinforces the formation of the CW LEV on the hind-wing, which results in increased peak lift and thrust. At the closest spacings, however; a jet forms between the two plates, which quickens the LEV shedding and results in a smaller and elongated LEV at the closest spacings. This behavior is most obvious when the spacing is decreased to 0.1c (which is shown in Fig. 14, rather than 0.25c).

3.2.3. Effect of vortex interaction on CP

The effect of the vortex interaction on the pressure distribution around the airfoil is shown in Fig. 15. The y-axis is reversed so that the top of the curve corresponds to the top of the airfoil (negative pressure) and vice versa. Fig. 15 compares the pressure distribution around the airfoil of both the single wing (a) and the hind wing at a phase angle of 0° and a wing spacing of 0.5c, (b) immediately before and immediately after the vortex interaction during the downstroke, which is the vortex interaction shown in Fig. 14. The hind-wing shows a large increase in suction at the top of the leading edge that corresponds with the passing of the vortex shed by the fore-wing. There is no observable increase in suction for the single wing at the same point in the cycle.

3.2.4. Effect of phase angle vs. spacing

Broering and Lian also investigated the relationship between phase angle and wing spacing [90]. Fig. 16 compares the transient

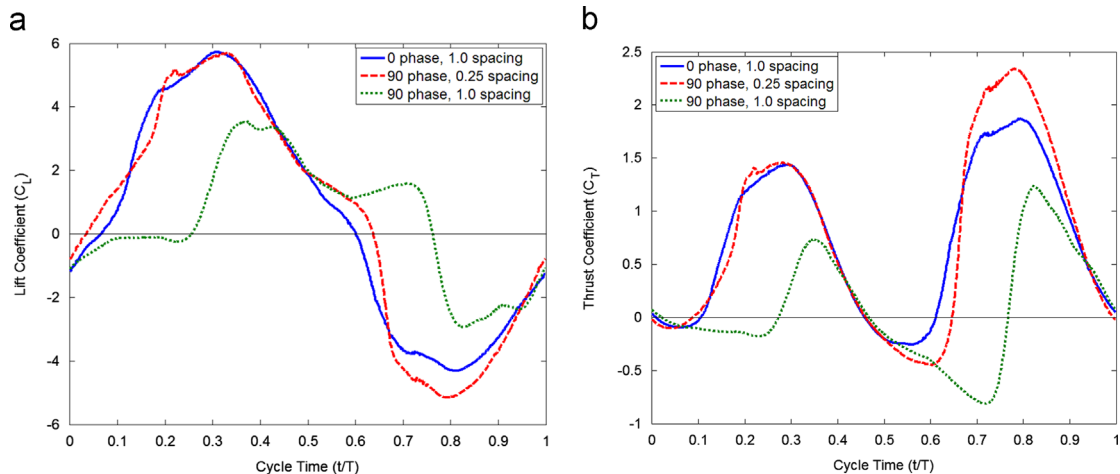


Fig. 16. Comparison of the lift and thrust over a single flapping cycle for the 0° hind-wing at 1.0c to the 90° hind-wing at 1.0c and 0.25c [50]. (a) Lift and (b) Thrust.

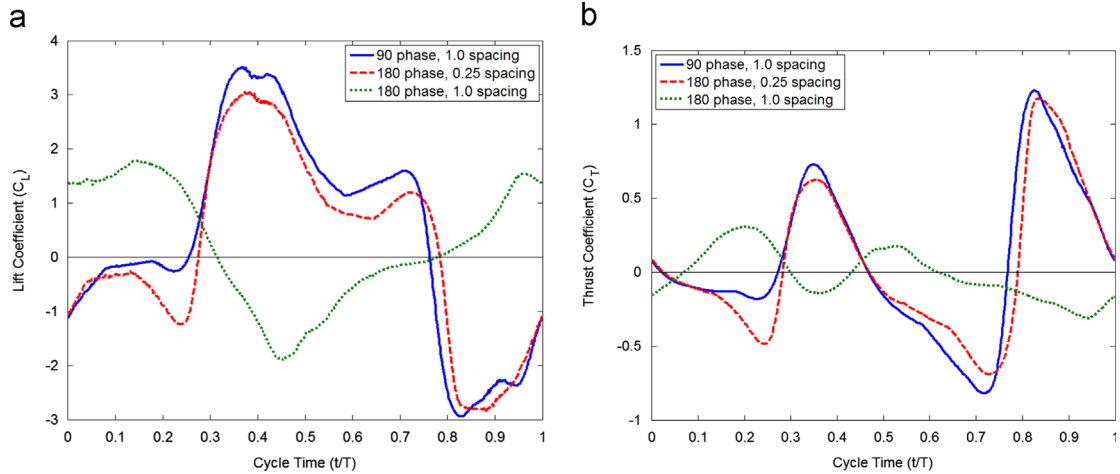


Fig. 17. Comparison of the lift and thrust over a single flapping cycle for the 90° hind-wing at 1.0c to the 180° hind-wing at 1.0c and 0.25c [50]. (a) Lift and (b) Thrust.

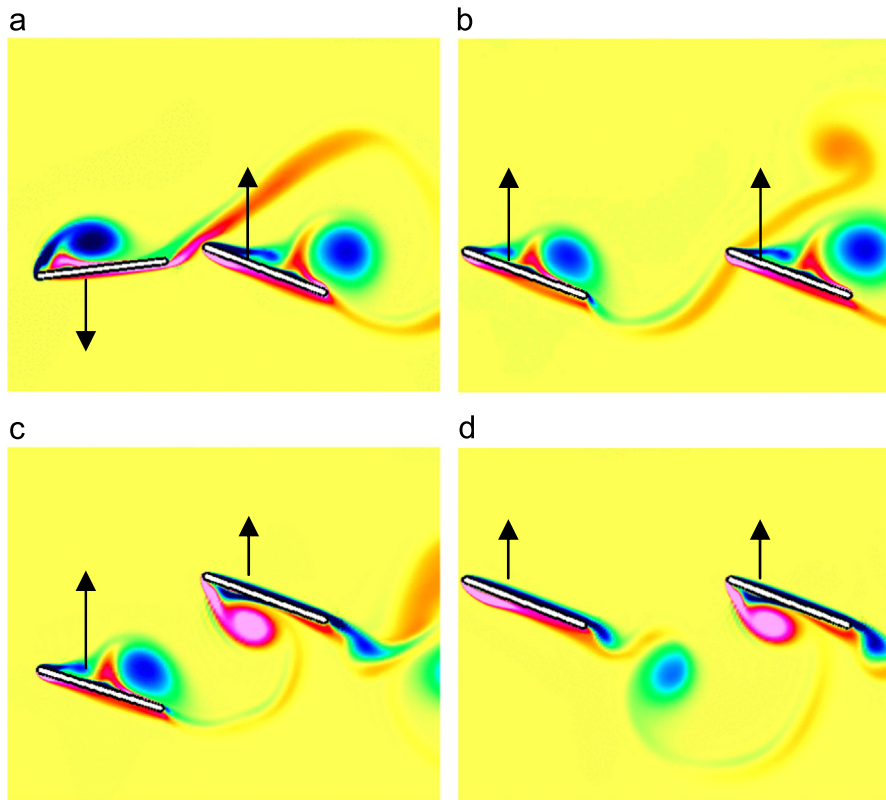


Fig. 18. Comparison of the vorticity contours for the 0° hind-wing at 1.0c to the 90° hind-wing at 0.25c and 0.1c [50]. Despite the parameter difference, the vortex structures on the hind wing are very similar. The contours were taken on the upstroke at 65% and 86% of the cycle time. Arrows indicate the stroke direction. (a) 90°, 0.25c, $t/T=65\%$, (b) 0°, 1.0c, $t/T=65\%$, (c) 90°, 0.25c, $t/T=86\%$ and (d) 0°, 1.0c, $t/T=86\%$.

lift and thrust history of the 0° phase angle case at 1.0c to the 90° case at 1.0c and 0.25c. Despite the difference in phase angle, the 0° case at 1.0c and the 90° case at 0.25c exhibit remarkably similar force histories. These two cases show nearly the same trend in lift and thrust generation (hence vortex and wing interactions) while the only difference between them is in peak lift and thrust production. This reveals that, in terms of force generation, decreasing the wing spacing has the opposite effect as increasing the phase angle. In this case, decreasing the baseline spacing from 1.0c to 0.25c while also increasing the baseline phase angle from 0° to 90° generates similar results as the baseline. However, when the phase angle is increased from 0° to 90° while keeping the

spacing constant at 1.0c, there is a significant change in the transient lift and thrust coefficient compared to the other two cases.

Fig. 17 is similar to Fig. 16, except it compares the force history of the 90° phase angle case at 1.0c to the 180° case at 1.0c and 0.25c. Again, the resulting force histories are very similar when the phase angle is increased by 90° while simultaneously decreasing the spacing from 1.0c to 0.25c. The two cases (90° at 1.0c and 180° at 0.25c) show similar timing in force generation, but different magnitudes of peak lift and thrust. Like Fig. 16, increasing the phase angle from 0° (1.0c) to 90° (1.0c) causes a shift in force histories. However, decreasing the spacing from 1.0c (90°) to 0.25c

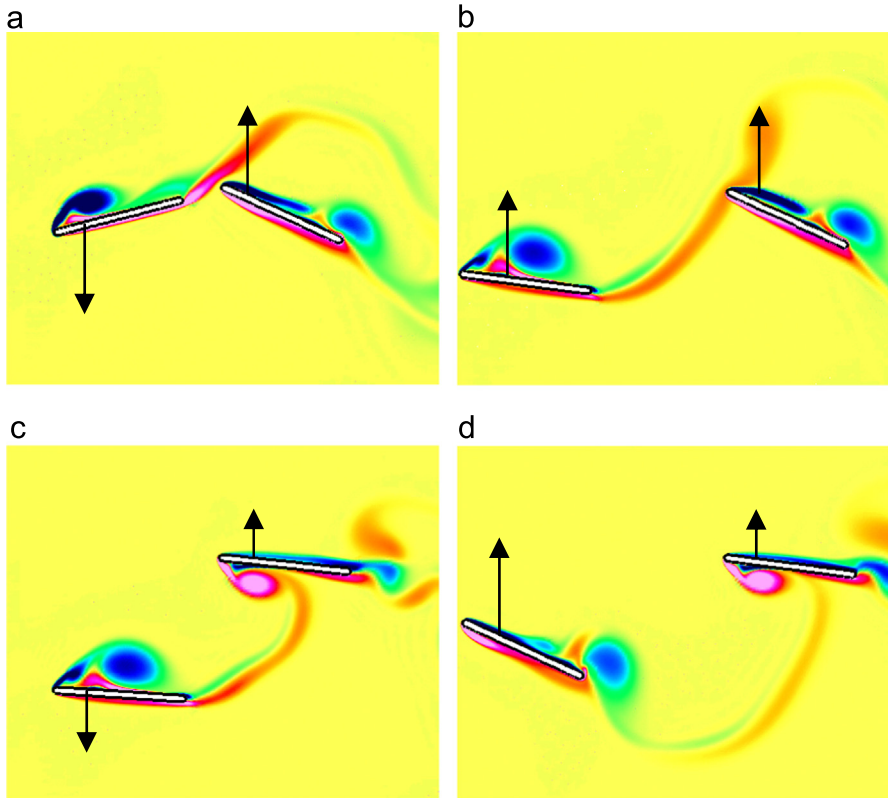


Fig. 19. Comparison of the vorticity contours for the 0° hind-wing at 1.0c to the 90° hind-wing at 0.25c and 0.1c [50]. Again, vortex structures on the hind-wing are very similar, despite the parameter difference. The contours were taken on the upstroke at 77% and 98% of the cycle time. Arrows indicate the stroke direction. (a) 180°, 0.25c, $t/T=77\%$, (b) 90°, 1.0c, $t/T=77\%$, (c) 180°, 0.25c, $t/T=98\%$ and (d) 90°, 1.0c, $t/T=98\%$.

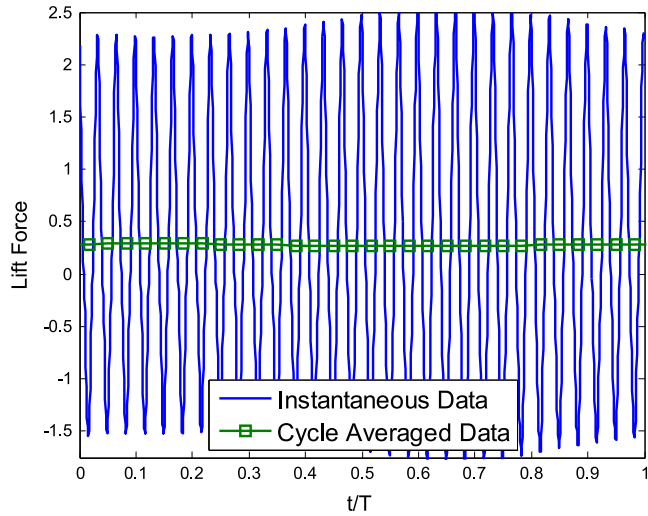


Fig. 20. Comparison of instantaneous and cycle averaged data [20].

(90°) will offset the shift. This shows that increasing the phase angle has the opposite effect as decreasing the spacing.

Examining the vorticity contours reveals why the force histories are nearly the same between the different cases. Fig. 18 compares the vorticity contours between the 0° and 90° cases at the different spacings during the upstroke. For these specific cases, the hind-wing passes through the vortex shed from the fore-wing at nearly the same time during the upstroke, which results in similar LEV generation on the hind-wing. Specifically, the timing of LEV generation and shedding is approximately the same among the two cases despite the difference in spacing and phase angle. This

corresponds to the similar force histories observed in Fig. 17. There are slight differences in the size of the LEV, which results in the difference in peak lift and thrust observed between the two cases.

Fig. 19 shows similar results to Fig. 18 for the 180° and 90° cases. For these two cases, though the phase angle and spacing are not the same, the timing of the vortex interaction between the fore and hind wings during the upstroke of the hind-wing is nearly identical. This results in comparable LEV formation on the hind-wing and the resulting similarities in the transient lift and thrust data between the 90° and 180° cases shown in Fig. 17. As with the 0° and 90° cases, there are slight differences in the size of the LEV generated, which result in the differences observed in the peak lift and thrust.

3.3. Conclusions

Previous studies suggested that the force production and efficiency of the hind wing are heavily influenced by its interaction with the wake of the fore wing, and that the nature of this interaction can be controlled by adjusting both the phase angle between the fore and hind wings and their spacing.

The interaction between the shed vortex and the hind wing also influences the LEV generation of the hind wing. Changes in the phase angle or spacing affect the timing of this interaction which, in turn, affects the timing of the generation and shedding of the LEV on the hind wing. The interaction between the shed vortex and the LEV can be described as constructive or destructive.

The timing of the LEV generation and shedding corresponds to the phase lag observed in the lift and thrust data associated with changes in the spacing and phase angle while the size of the LEV generated corresponds to the peak lift and thrust production. This suggests that changes in the phase angle and spacing can be used to control the force production and efficiency of the hind wing by

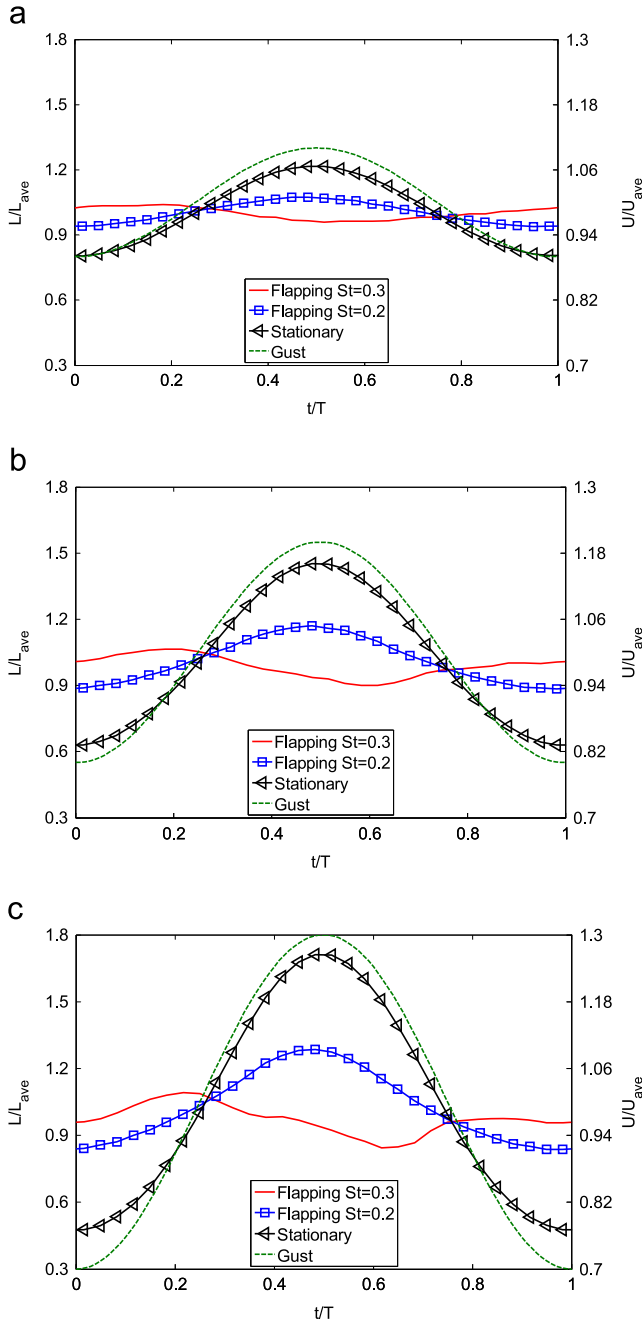


Fig. 21. Comparison of lift over a single gust cycle at different gust amplitudes and Strouhal numbers between flapping and stationary flat plate [20]: (a) 10% gust, (b) 20% gust and (c) 30% gust.

controlling its LEV formation. Both the phase angle and spacing were observed to have similar effects on the force production, which corresponded to similarities in the LEV formation and shedding.

4. Tandem wing and wind gust

Prater and Lian [20] studied the aerodynamics of tandem wings under gusty conditions. Since the wind gust profile can be complicated and the complexity of urban layout further makes it difficult to model analytically, they used a simple wind gust model with single frequency harmonic oscillation. The oscillation was further limited to the horizontal direction (x -direction). Such

a wind gust model is described by

$$U(t) = U_{ave}(1 + A \cos(2\pi f_{gust} t)) \quad (21)$$

where U_{ave} is the mean freestream velocity, A the amplitude of freestream oscillation, and f_{gust} is the gust frequency. The flapping airfoil experiences a single frequency pitching and plunging motion described by

$$\theta(t) = \theta_{amp} \cos(2\pi f_{flap} t + \phi_\theta) + \theta_{ave} \quad (22)$$

$$h(t) = h_{amp} \cos(2\pi f_{flap} t + \phi_h) + h_{ave} \quad (23)$$

where θ_{amp} and h_{amp} are the pitch and plunge amplitude, θ_{ave} and h_{ave} are the average angle of attack and plunge amplitude, f_{flap} is the flapping frequency, and ϕ is the phase angle.

In their study the Reynolds number ($Re = \rho U_{ave} c / \mu$) based on airfoil chord length and averaged wind speed was 500. For the flapping kinematics a reduced flapping frequency, k , of 0.2 was used, the pitch amplitude, θ_{amp} , was 10° and the average angle of attack, θ_{ave} was 6° . The ratio between the flapping frequency and wind gust frequency was 30 which is representative of the real world characteristics for hummingbirds or insects whose flapping frequency is much higher than the gust frequency. The gust amplitude, U_{amp} , was between 0 and 0.3.

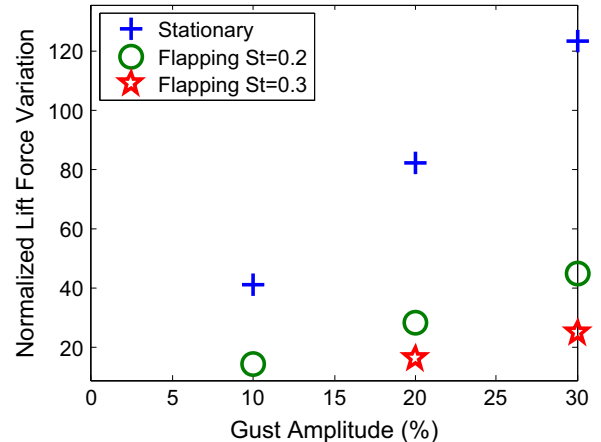


Fig. 22. Comparison of peak-to-peak lift variation between stationary and flapping plate at different gust amplitudes [20].

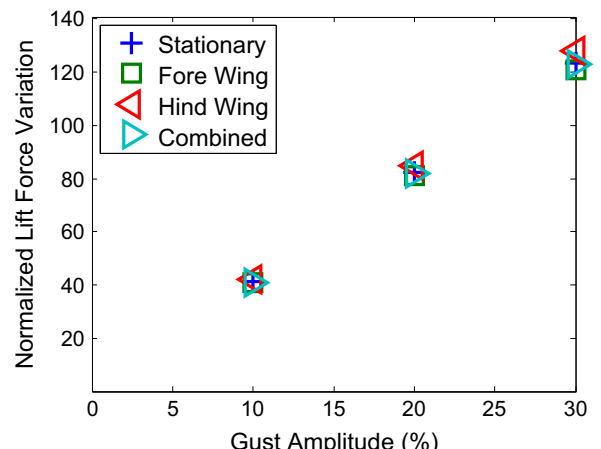


Fig. 23. Comparison of the force results for tandem stationary wings separated by a full chord [20].

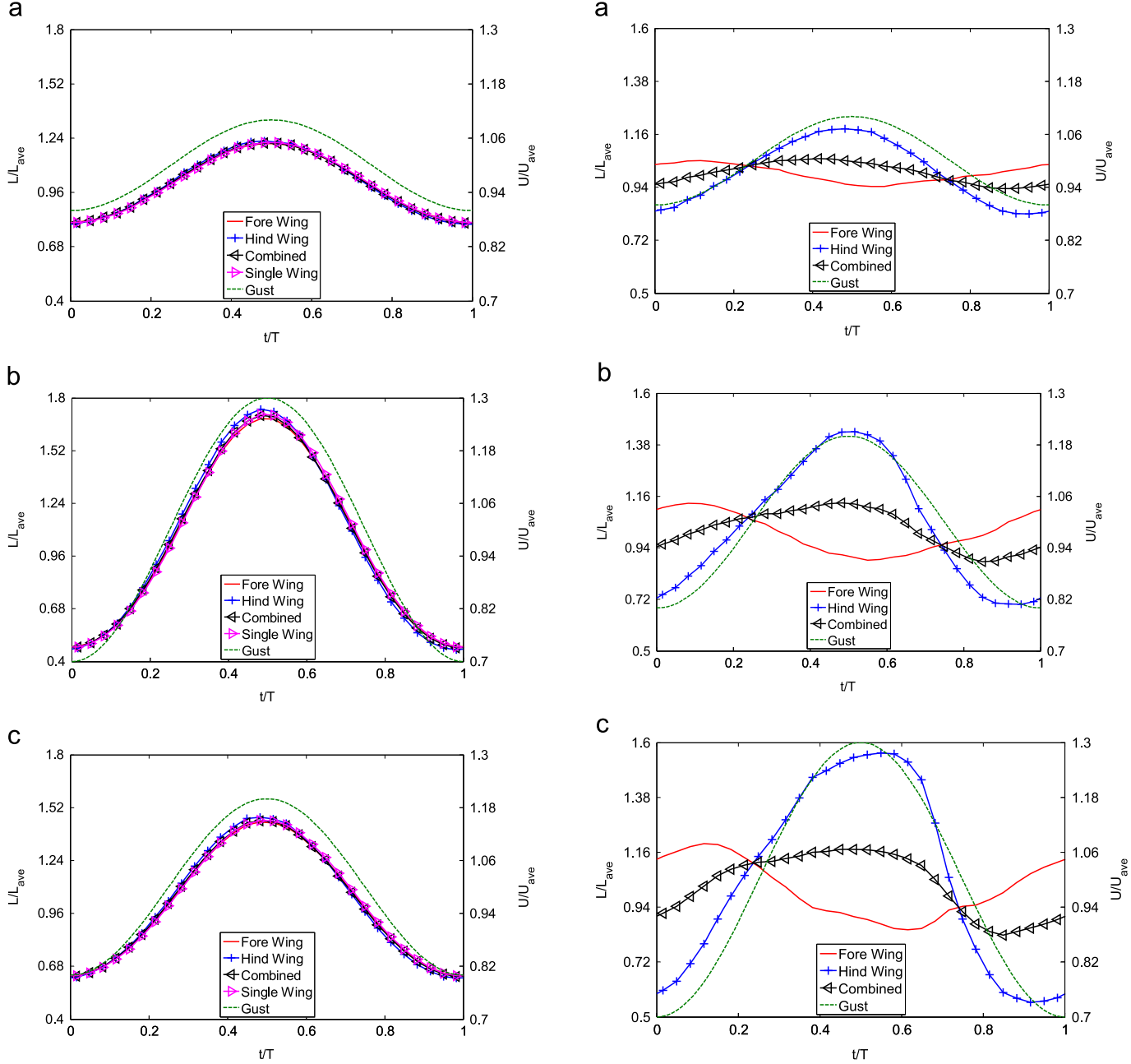


Fig. 24. Comparison of the lift history over one gust cycle at different oscillation amplitudes [20]. In the tandem wing configuration both fore and hind wings are stationary and have an angle of attack of 6°: (a) 10% gust, (b) 20% gust and (c) 30% gust.

4.1. Single wing results

Prater and Lian [20] compared the performance of a stationary flat plate and a flapping flat plate in oscillatory flows. Three oscillation amplitudes ($A=0.1, 0.2, 0.3$) were tested. For the flapping cases two different Strouhal numbers (0.2 and 0.3) were used. The selected Strouhal numbers fall into the range of natural flyers suggested by Taylor et al. [91]

As argued by Sun et al. that because the wing beat frequency is much higher than the natural oscillatory frequency of the MAV, the MAV can be treated as a rigid body with only 6 degrees of freedom, i.e., the wings' degrees of freedom relative to the body are ignored [92]. Under that assumption the time-variant forces, moments and moments of inertia are cycle averaged out over each

Fig. 25. Comparison of the lift history over one gust cycle at different gust oscillation amplitudes [20]. In the tandem wing configuration the fore-wing is flapping and hind-wing is stationary: (a) 10% gust, (b) 20% gust and (c) 30% gust.

wing beat cycle and make a constant contribution to the body during a wing beat cycle. Fig. 20 shows both the time instantaneous and flapping cycle averaged lifts over one gust cycle. The instantaneous force exhibits a larger variation than the cycle averaged force, however because of the high flapping frequency only the flapping cycle averaged force affects the flat plate.

The lift history over one gust cycle is shown in Fig. 21. The shown lift is normalized by the gust cycle averaged lift. The reported data is collected when a periodic behavior is observed over gust cycles. For comparison purpose, the lift history of the stationary plate under same gust is reported. At a gust amplitude of 0.1 the stationary plate shows a peak-to-peak variation of 41.2% but variation from the flapping airfoil at $St=0.2$ and 0.3 is 14.4% and 8.2%, respectively, representing a reduction of 67.1% and 70.1% from the stationary airfoil. When the gust amplitude increases to 0.2 the peak-to-peak variation

of the stationary airfoil is more than 82%, and the variation for the flapping plate at $St=0.2$ and 0.3 is 28.5% and 16.4%, respectively, a reduction of 65.3% and 80.0%. The same trend is also observed at the gust amplitude of 0.3. In Fig. 22 the peak-to-peak lift variation between the stationary and flapping flat plates are compared. Overall the peak-to-peak variation increases with the gust amplitude.

Another interesting phenomenon is observed in Fig. 21. The lift history of the stationary plate and the flapping plate at $St=0.2$ follows the freestream wind variation while the lift force of the flapping plate at $St=0.3$ does not follow the freestream gust variation instead, there is a lag of approximately 270° between the wind variation and lift in all the three different oscillation amplitude cases.

4.2. Tandem wing results

Nagai et al. [93] showed through experimental studies that proper adjustment of the relative motion of the fore and hind wings can stabilize the flight. Numerical study of the gust impact on tandem wings was conducted by Prater and Lian [20]. In their work three tandem configurations were selected. The first one consisted of two stationary wings; the second configuration consisted of one flapping fore-wing and one stationary hind-wing, both of which were represented by flat plates to maintain consistency within this study. The third case imposed the flapping motion on the hind-wing while the fore-wing remained stationary. The major observations are summarized in the following sections.

4.2.1. Case 1: Two stationary wings in tandem configuration

The two wings are separated by a single chord length. Both of them have a fixed angle of attack of 6°. The lift variation with the freestream velocity is shown in Fig. 23. Comparisons are also made with single isolated wing under the same simulation parameters. The fore-wing and hind-wing have similar normalized peak-to-peak lift variation. This variation is also similar to a single flat plate in isolation.

Fig. 24 shows the normalized lift force history of the fore-wing, hind-wing, combined wings, and the single wing in isolation. When normalized by their corresponding averaged lift, these four lift curves are almost identical, indicating the wind gust affects two stationary flat plates in tandem configuration the same way as it would affect a single flat plate in isolation. Lift variation closely follows the variation of gust velocity squared.

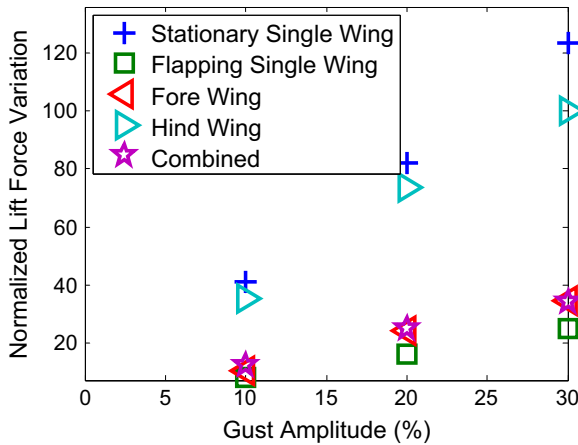


Fig. 26. Comparison of lift variation over a gust cycle at different gust amplitudes. In the tandem wing configuration the two wings are one-chord apart and the fore wing is flapping and hind wing is stationary. The flapping wings generally show less variation than stationary wings.

Prater and Lian [20] also tested a stationary tandem wing case with a spacing of 0.5 chords. One noticeable change is that in the new configuration the hind-wing contributes less (~28%) of the total force instead of 31% in the one-chord separation case. However, the normalized peak-to-peak variation for fore-wing, hind-wing, and combined is nearly identical to the case with the one full chord separation.

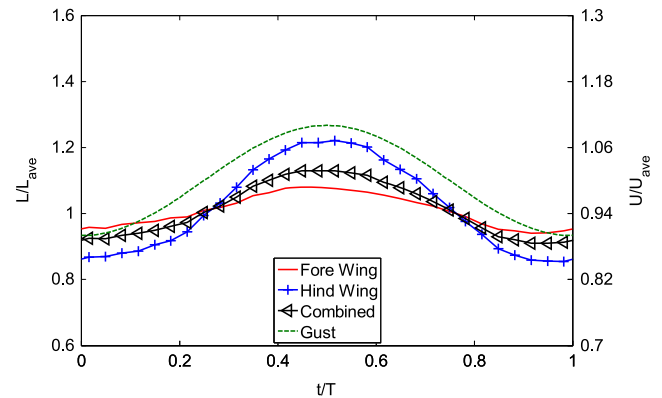


Fig. 27. Lift history of fore-wing, hind-wing, and combined wings over one gust cycle with 10% wind gust. Two wings are half-chord apart and the fore-wing is flapping and hind-wing is stationary.

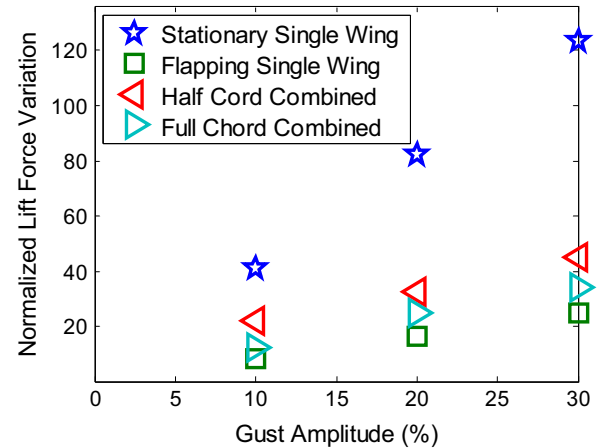


Fig. 28. Impact of spacing between fore- and hind-wings in tandem configuration. Fore-wing is flapping and hind-wing is stationary.

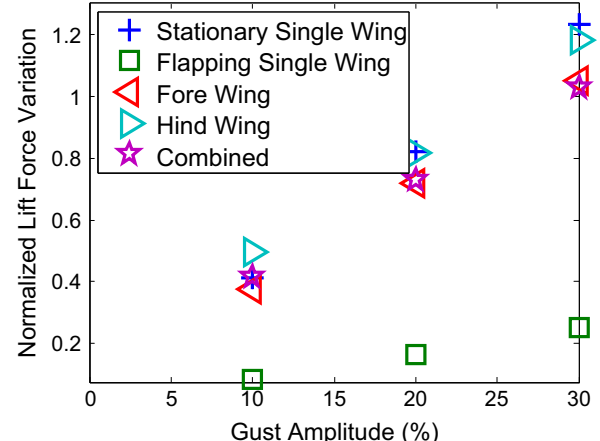


Fig. 29. Comparison of the peak-to-peak lift variation for a stationary fore-wing and flapping hind-wing at different gust conditions. The two tandem wings are at a full chord separation [20].

4.2.2. Case 2: Flapping fore-wing and stationary hind-wing

In this configuration the fore-wing is flapping at a Strohal number of 0.3 and the hind-wing is stationary. Fig. 25 compares the force histories for the fore-wing, hind-wing and combined wings over a single wind gust cycle. In all three gust amplitudes the hind-wing shows larger variation than the fore-wing. Interestingly, the hind-wing's lift variation follows the wind gust but the fore-wing's lift variation lags the wind gust by nearly 180° . When the hind-wing reaches the peak lift, the fore-wing is near its trough and vice versa. The phase difference between the fore- and hind-wing helps to reduce the variation in the combined force. Additionally it can be seen that the hind-wing's peak becomes less sharp and more elongated as the gust amplitude increases. In this tandem configuration the fore-wing contributes a larger percentage ($\sim 69\%$) of the total force than the hind-wing ($\sim 31\%$) which is why the trends for the combined forces are closer to the flapping wing trends than the stationary wing trends, i.e. the combined forces exhibit lower force variations than a stationary wing.

Comparisons are also made with a stationary wing and a flapping wing in isolation. Fig. 26 shows the force variation over one gust period when two wings are separated by one chord. Among all the cases the single stationary wing has the highest peak-to-peak variation while the single flapping wing has the lowest. In general the flapping wings show much less variation than stationary wings. The variation for the combined fore-wing and hind-wing is similar to the flapping single wing case.

Prater and Lian [20] further investigated the impact of wing gap on the tandem wing performance in gusts. One difference between the one-chord configuration and the half-chord configuration is that in the half-chord tandem configuration the lift variation of the fore and hind wing follows the gust variation (Fig. 27) while the one-chord configuration shows nearly 90° phase lag between the fore and hind wing (Fig. 25).

Fig. 28 shows the variation compared to the configuration with a full chord separation. The half-chord configuration shows slightly higher peak-to-peak lift variation in the combined force.

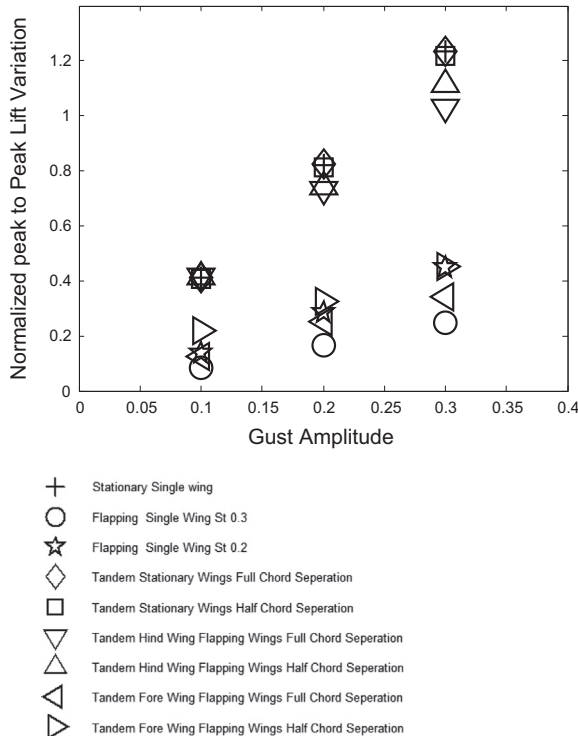


Fig. 30. Summary of different wing configurations under gusty conditions.

4.2.3. Case 3: Stationary fore-wing and flapping hind-wing

This tandem configuration has a stationary fore-wing and a flapping hind-wing ($St=0.3$). Fig. 29 summarizes the computed results for this configuration when there is a full chord separation. For this configuration, as in the first configuration where both wings are stationary, the fore-wing contributes about 75% of the total force. It is also noted that this configuration is less effective in alleviating the oscillation variation. Large variations are recorded in all three oscillation amplitudes tested. Different wing spacings are tested but the change in the lift variation compared to the one chord case is fairly small (less than 2%).

4.3. Conclusions

Different configurations can play a remarkably profound role in both the variation and lift generation in response to flow at varying oscillation amplitudes. As summarized in Fig. 30 a flapping wing generally experience less peak-to-peak lift variation than a stationary wing. The only case where this not observed is the case where the flapping wing is located behind the stationary wing. If a tandem wing configuration is used the location of the wings and whether the fore or hind wing was flapping plays a great role in the percentage reduction/increase. From the cases studied the tandem wing case with a fore wing flapping and stationary hind wing was

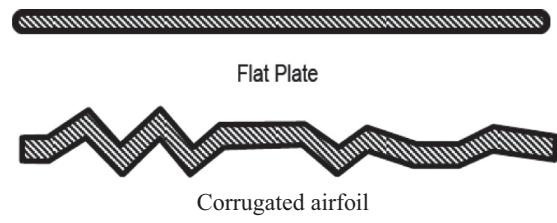
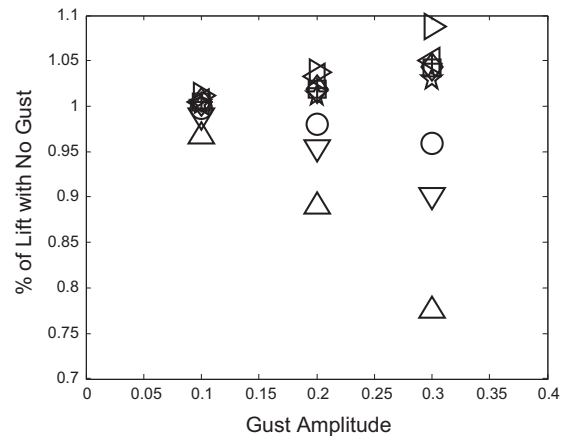


Fig. 31. Test airfoil profiles.



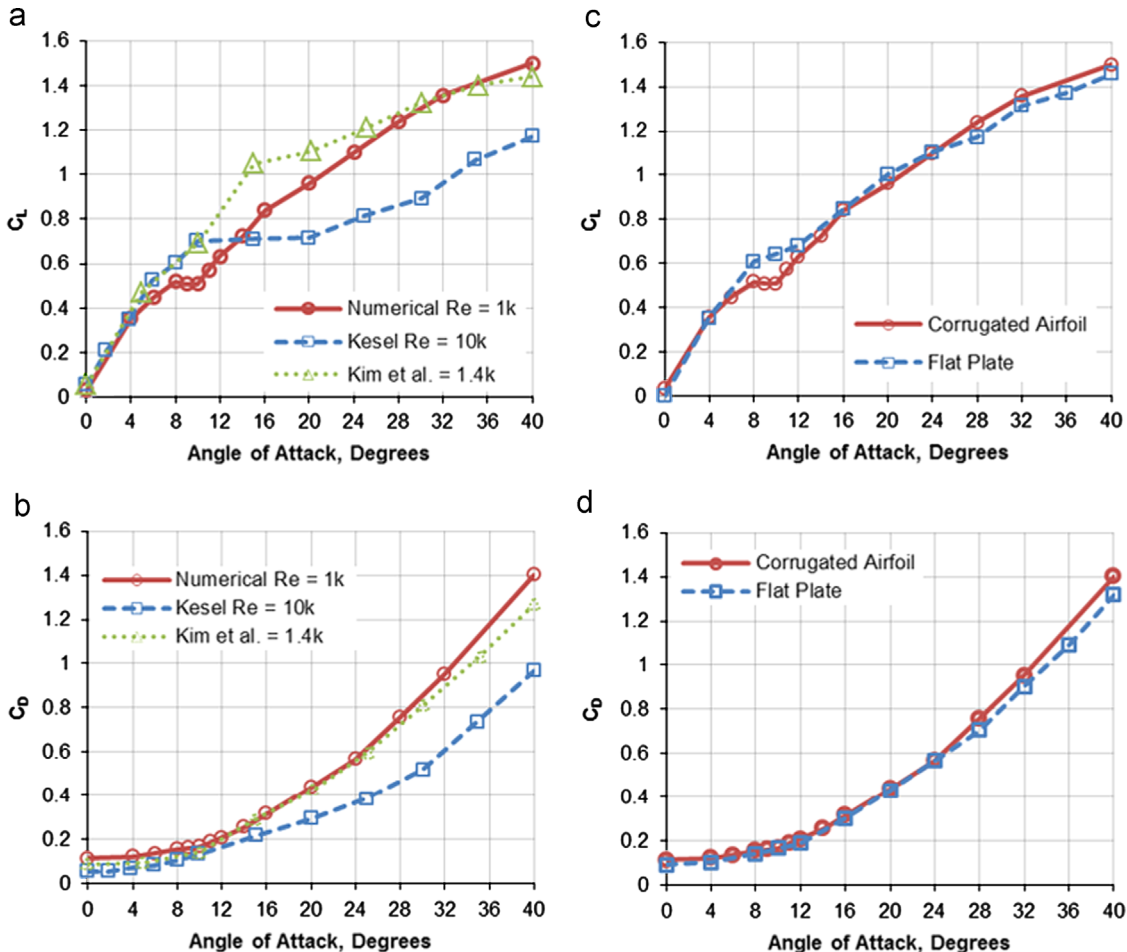


Fig. 32. Numerical results of corrugated profile plotted against published data [76].

the best at minimizing the variation of the forces encountered while maximizing the lift generated in increasing oscillations.

5. Corrugated wing performance

Hord and Lian [76] studied the corrugated wing performance. Fig. 31 shows the two profiles they tested, a flat plate and a corrugated airfoil. The profile of the corrugated airfoil was taken from the fore-wing of an *A. cyanea* dragonfly. The original profile was developed by Kesel [70] and then taken by Murphy and Hu [71] who gave a thickness to the airfoil. The flat plate has a round leading and trailing edges. The flat plate and corrugate airfoil have the same chord length and thickness of 2% of the chord. The chord based Reynolds number was 1000.

5.1. Effect of angle of attack

In their work the effect of angle of attack on aerodynamic forces was first investigated. The calculated coefficients of lift are plotted against experimental data from Kesel [70] at Re equal to 10,000 and numerical data from Kesel et al. [75] at Re equal to 1400 in Fig. 32(a). Since vortex shedding occurs at modest angles of attack, the results plotted are the time averaged coefficient of lift. They prediction is very close to the experimental data at low angles of attack ($\alpha \leq 4^\circ$). Because of the disparity of Reynolds number, the closeness seems to indicate the lift is not sensitive to the Reynolds number at low angles of attack. At modest angles of

attack there is a disagreement between Kim et al.'s and their numerical data. They attributed the deviation from Kim et al.'s to the difference in corrugate profiles used.

Examining Fig. 32(b) shows that the numerical results derive from experimental results of Kesel. This can be attributed to more prominent viscous effect at lower Reynolds numbers. Comparison with the flat plate is shown in Fig. 32(c) and (d). The corrugated wing and the flat plate produce very similar lift at almost all the angles of attack, which is consistent with Kesel's finding which concludes that the corrugated profile acts much like a flat plate. The corrugated profile produces slightly higher drag than the flat plate. The slight difference in lift between the corrugated profile and flat plate may be due to the difference in leading and trailing edges. The corrugated profile has sharp edges, while the flat plate has rounded ones.

5.2. Effects of corrugation

To further understand the flow physics, Hord and Lian [76] examined the streamlines around the corrugated airfoil. They found that near stagnant rotating flow was trapped within the valleys. Due to trapped vortices, the corrugated airfoil acts like a thick and smooth airfoil.

Fig. 33 shows the virtual profile around the corrugation compared to the flat plate at various angles of attack. The increase in virtual thickness of the airfoil increases the pressure drag. The flat plate does not show a virtual profile thickness increase until at approximately 8° . When the angle is less than 8° , the flow sticks to

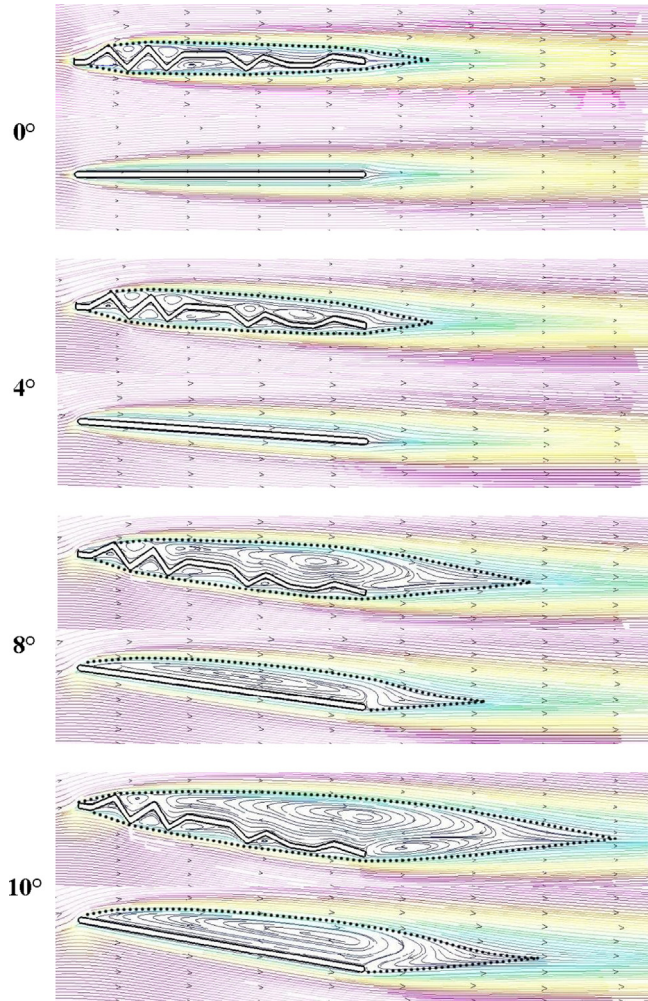


Fig. 33. Steady flow streamline visualization around the corrugated profile. Virtual profile represented by dotted line.

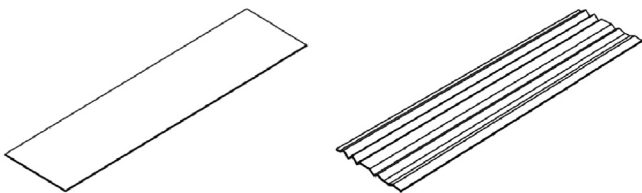


Fig. 34. The flat plate and corrugated wing models used [76].

the surface of the flat plate, while the flow conveys across the vortices in the corrugated airfoil. This delay in virtual profile development reduces pressure drag, while the rotating flow in the valley results in the production of negative viscous drag that reduces the total drag caused by shear.

At 8°, the coefficient of drag for the corrugated airfoil and the flat plate are 0.156 and 0.141 respectively. The viscous drag makes up only 17% of the total drag on the corrugated airfoil, while the viscous drag makes up 30% of the drag on the flat plate. This effectively shows that the corrugated airfoil has lower viscous drag. However, because of the thick virtual profile produced by the trapped vortices, the pressure drag on the corrugated airfoil is 1.34 times higher than the flat plate's pressure drag. This increase in drag reduces the lift-to-drag ratio. Both the flat plate and the corrugated airfoil produce peak lift-to-drag ratios, (C_L/C_D)_{max}, around 8°. The peak lift-to-drag ratio of the flat plate and the corrugated airfoil are 4.3 and 3.3 respectively.

The numerical simulations by Hord and Lian [76] demonstrate that the corrugated airfoil acts similar in lift production as a flat plat, however it produces more drag, which agrees with Kesel [70]. They attributed the increase to the near stagnate rotating vortices which make the corrugated airfoil function like a thick and cambered streamlined airfoil. The airfoil thickness and camber increase the pressure drag. The increase in pressure drag is partially offset by the decrease in viscous drag due to the negative shear stresses in the valleys, leading to a net increase of total drag. This increase in drag reduces lift-to-drag ratio significantly. This evidence seems to indicate that the corrugated airfoil is not intended for aerodynamic improvement, but instead for structural benefits as previously hypothesized by other researchers [68,69].

5.3. Structural analysis

Hord and Lian [76] also performed structural simulation tests similar to Kesel et al.'s [75] finite element analysis based on the *A. cyanea* fore-wing. Instead of testing the fore-wing, Hord and Lian created a 3D homogeneous profile of the wing span to test the structural properties of the corrugated profile. The corrugated wing was then compared to a flat plate wing span. Each wing was created using the SolidWorks 2009 [94] designer, and then tested using the program's own structural simulation tools.

In their work the 3D wing was given the properties of Chitin. Each model was assumed to have a material with an isotropic nature. The properties of Chitin were taken from Kesel et al. [75] which list Young's modulus as 6.1 GN/m² and an assumed Poisson's ratio of 0.25. Each model was then subjected to a pressure load of 4.061×10^{-6} GN/mm², which provides a homogenous wing loading that approximates the weight of the dragonfly. Several models of the corrugation and flat plate were created, varying the percent thickness of each from 1% to 6%. Each wing had a chord length of 1 cm and span of 4 cm, which are approximations of the dimensions of the *A. cyanea* fore-wing. Fig. 34 shows a sample of the models produced.

The maximum displacement of the various profile thicknesses of the flat plate and corrugated profile were measured. In Fig. 35(a) graphs the displacement of each thickness. The flat plate shows little resistance to displacement at its thinnest thickness. The 1% flat plate deflects approximately 2.5 mm under load. However, the corrugated profile demonstrates a much higher rigidity in comparison. Its deflection was 35 times lower than the flat plate. Table 1 details the deflection reduction between the corrugated profile and the flat plate at each thickness. Past a 3% thickness, the flat plate shows little improvement on deflection reduction while the corrugated wing shows little to no change.

A similar trend is seen with the average stress across the wings as previously seen with the deflection. The flat plate shows much higher average stress at lower thicknesses, but past 3% the reduction of stress decreases slower as the thickness increases. In Fig. 35(b) graphs the average stress on each wing. At 1%, the corrugated wing shows a reduction of stress by a factor of 8. The corrugation again shows its superior ability to handle loading more efficiently than the flat plate without increasing the thickness of the wing. Like the deflection trend, the stress reduction ratio also begins to fall, as plate thickness increases. Table 7 shows the stress reduction at each thickness.

Table 7 details the equivalent percent thickness required for the flat plate to match the performance of the corrugated wing at each thickness ratio. It would take a 3.16% flat plate to match the displacement of a 1% corrugated wing.

5.4. Conclusions

Numerical simulations showed that the corrugated airfoil produces similar lift as a flat plate, but at peak gliding ratios, it produces more

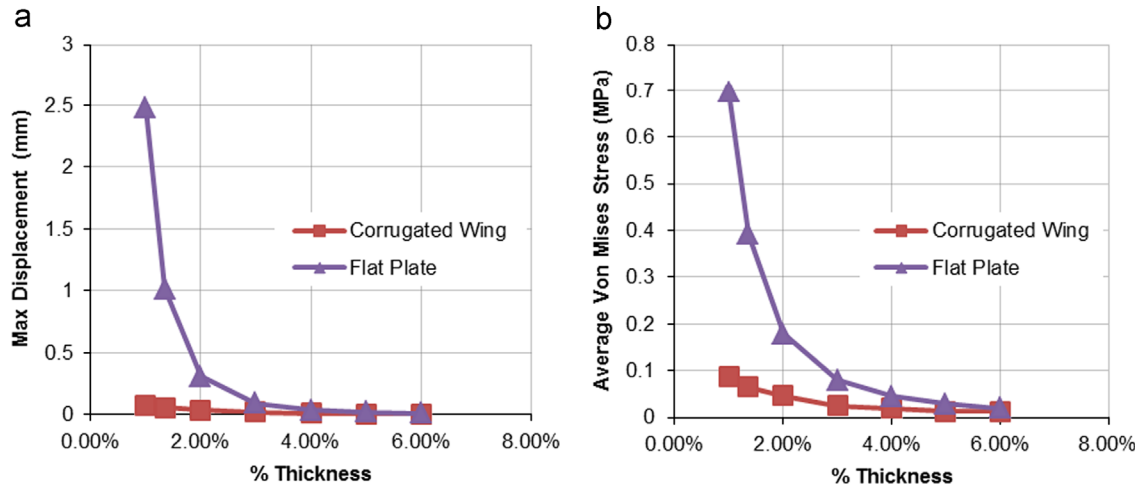


Fig. 35. (a) Maximum displacement of models and (b) average Von Mises stress.

Table 7
Equivalent thickness of flat plate to match performance of the corrugated wing.

Corrugated wing thickness (%)	Reduction ratio		Equivalent flat plate Thickness	
	Displacement	Stress	Displacement (%)	Stress (%)
1.00	35.92	8.09	3.16	2.87
1.35	19.87	5.96	3.53	3.29
2.00	9.08	3.88	4.11	3.93
3.00	4.60	3.21	4.94	5.37
4.00	2.96	2.28	5.75	6.05
5.00	2.25	2.12	6.57	7.31
6.00	1.87	1.60	7.42	7.62

drag. The increase in drag is due to the higher pressure drag resulting from the thicker virtual streamlined profile created by the stagnant vortices trapped in the valley. The higher pressure drag is partially offset by the negative shear stresses from the rotating vortices. The lift oscillations of both the flat plate and the corrugated profile were identical with similar vortex shedding frequencies at higher angles of attack. It shows that the corrugations do not interfere with the vortex shedding. However, compared with a flat plate, the flat plate produces more favorable aerodynamic characteristics. Overall, the corrugated profile provides no advantages in terms of stall delay or lift generation at low Reynolds numbers. Investigating the structural properties of the corrugated wing and flat plate showed that, under a static loading, the corrugated wingspan has superior performance compared with the flat plate in terms of bending resistance. The corrugated wing can reduce deflection and stress on the wing. It would take a flat plate with three times the thickness to perform as well as the corrugated wing.

6. Conclusions

There is no doubt that significant progress has been made in the study of tandem and corrugated wings. However, considerable research in the following areas is required to fully understand the tandem and corrugated wing characteristics:

(a) *Force measurement of tandem wings:* Lots of experiments have been carried out to measure forces on single wings but there is limited force measurement on tandem wings. Instead of using real complex kinematics similar to those of dragonflies, a

simple kinematics should be adopted in the experiment. A simple kinematics like the pure pitching or plunging motion is preferred because it can not only reveal the pertinent fluid mechanics features in tandem wing configuration such as dynamic stall and vortex/wing interactions but provide canonical cases that CFD practitioners can benchmark their codes.

(b) *Force measurement under gust conditions:* Only a few papers have been published to discuss the fixed wing performance under gust conditions. Given the large difference between the gust frequency and flapping frequency, no experimental work has been reported to understand the flapping wing performance under gust conditions.

(c) *Three-dimensional effects:* On a finite aspect ratio wing, the leading edge vortex is affected by the spanwise flow and also by tip vortices. The hind wing is also affected by the tip vortices shed from fore wing. Tremendous CPU hours are needed to resolve the tip effects. For corrugated wings the corrugation patterns and leading edge orientation of dragonflies are different along the spanwise. Further studies are needed to understand whether this spanwise variation can affect the wing aerodynamics.

(d) *The control of vortex-vortex interactions:* In general we know that constructive vortex interactions increase the thrust while destructive interactions increase the propulsive efficiency. However, more work is needed to understand the role of each parameter (spacing, frequency, amplitude, phase lag, and Reynolds number) to eventually be able to control the occurrence of these interactions.

(e) *A thorough understanding of the flapping motion and gust modulation:* The role of flapping motion on the gust modulation is still not clear. The method proposed by Jones et al. [95] could be a useful tool for that purpose

References

- [1] Shyy W, Lian Y, Tang J, Viieru D, Liu H. Aerodynamics of low reynolds number flyers. Cambridge University Press; 2008.
- [2] Lian Y, Shyy W, Viieru D, Zhang B. Membrane wing aerodynamics for micro air vehicles. Prog. Aerosp. Sci. 2003;39(6):425–65.
- [3] Shyy W, Lian Y, Tang J, Liu H, Trizila P, Stanford B, et al. Computational aerodynamics of low Reynolds number plunging, pitching and flexible wings for MAV applications. Acta Mechanica Sinica 2008;24(4):351–73.
- [4] Ifju PG, Jenkins DA, Ettinger S, Lian Y, Shyy W, Waszak MR. Flexible-wing-based micro air vehicles. AIAA Pap. 2002;705(2001-3290):1–11.
- [5] Grasmeyer JM, Keenon MT. Development of the black widow micro air vehicle. Progress in Astronautics and Aeronautics 2001;195:519–35.

- [6] Porsin-Sirak TN, Tai Y-C, Ho C-M, Keenon M, editors. Microbat: a palm-sized electrically powered ornithopter. In: Proceedings of NASA/JPL workshop on biomimetic robotics; 2001.
- [7] McMasters JH, Hendersen ML. Low speed single element airfoil synthesis. Technical Soaring 1980;6:2.
- [8] Pines DJ, Bohorquez F. Challenges facing future micro-air-vehicle development. *Journal of Aircraft* 2006;43(2):290–305.
- [9] Platzer MF, Jones KD, Young J, Lai S, Flapping JC. Wing aerodynamics: progress and challenges. *AIAA Paper* 2008;46(9):2136–49.
- [10] Shyy W, Berg M, Ljungqvist D. Flapping and flexible wings for biological and micro air vehicles. *Prog. Aerosp. Sci.* 1999;35(5):455–505.
- [11] Li T, Zhu D, Law C. Droplet combustion, microexplosion, and sooting characteristics of several energetic liquid propellants. *Journal of Propulsion and Power* 1998;14(1):45–50.
- [12] Li T, Zhu D, Akafuah N, Saito K, Law C. Synthesis, droplet combustion, and sooting characteristics of biodiesel produced from waste vegetable oils. *Proceedings of the Combustion Institute* 2011;33(2):2039–46.
- [13] Jones K, Platzer M. Numerical computation of flapping-wing propulsion and power extraction. *AIAA Paper* 1997;97:0826.
- [14] Taylor GK, Nudds RL, Thomas ALR. Flying and swimming animals cruise at a Strouhal number tuned for high power efficiency. *Nature* 2003;425(6959):707–11.
- [15] Knoller R. Die Gesetze des Luftwiderstandes. *Flug- und Motortechnik* (Wien) 1909;3:21.
- [16] Betz A. Ein Beitrag zur Erklärung des Segelfluges. *Zeitschrift für Flugtechnik und Motorluftschiffahrt* 1912:3.
- [17] Young J, Lai JC, Platzer MF, Srinivas K, Freymuth P, Koochesfahani MM, et al. Oscillation frequency and amplitude effects on the wake of a plunging airfoil. *AIAA Journal* 2004;42(10):2042–52.
- [18] Garrick I. Propulsion of a flapping and oscillating airfoil. National Bureau of Standards; 1936.
- [19] Ramamurti R, Sandberg W. Simulation of flow about flapping airfoils using finite element incompressible flow solver. *AIAA Journal* 2001;39(2):253–60.
- [20] Prater R, Lian YS. Aerodynamic response of stationary and flapping wings in oscillatory Reynolds number flows. *AIAA Paper* 2012-0418; 2012.
- [21] May ML. Dragonfly flight: power requirements at high speed and acceleration. *Journal of Experimental Biology* 1991;158:325–42.
- [22] Reavis MA, Luttges MW. Aerodynamic forces produced by a dragonfly. *AIAA Journal* 1988;1:13.
- [23] Dong H, Koehler C, Liang Z, Wan H, Gaston Z. An integrated analysis of a dragonfly in free flight. *AIAA Paper* 2010-4390 2010;4390:1–10.
- [24] Schmidt W. Der Wellpropeller, ein Neuer Antrieb fuer Wasser-, Land-, und Luftfahrzeuge. *Zeitschrift für Flugwissenschaften* 1965;13:427–79.
- [25] Bosch H. Interfering airfoils in two-dimensional unsteady incompressible flow. AGARD unsteady aerodynamics, SEE N 78-22033 13-02; 1978. 15 pp.
- [26] Tuncer IH, Platzer MF. Thrust generation due to airfoil flapping. *AIAA Journal* 1996;34(2):324–31.
- [27] Alexander D. Unusual phase relationships between forewings and hindwings in flying dragonflies. *Journal of Experimental Biology* 1984;109:379–83.
- [28] Ruppell G. Kinematic analysis of symmetrical flight maneuvers of Odonata. *Journal of Experimental Biology* 1989;144:13–42.
- [29] Azuma A, Watanabe T. Flight performance of a dragonfly. *Journal of Experimental Biology* 1988;137(1):221–52.
- [30] Thomas ALR, Taylor GK, Srygley RB, Nudds RL, Bomphrey RJ. Dragonfly flight: free-flight and tethered flow visualizations reveal a diverse array of unsteady lift-generating mechanisms, controlled primarily via angle of attack. *Journal of Experimental Biology* 2004;207(24):4299–323.
- [31] Lan CE. The unsteady quasi-vortex-lattice method with application to animal propulsion. *Journal of Fluid Mechanics* 1979;93(4):747–65.
- [32] Usherwood JR, Lehmann FO. Phasing of dragonfly wings can improve aerodynamic efficiency by removing swirl. *Journal of the Royal Society Interface* 2008;5(28):1303–7.
- [33] Maybury W, Lehmann FO. The fluid dynamics of flight control by kinematic phase lag variation between two robotic insect wings. *Journal of Experimental Biology* 2004;207:4707–26.
- [34] Yamamoto M, Isogai K. Direct measurement of unsteady fluid dynamic forces for a hovering dragonfly. *AIAA Journal* 2005;43(12):2475–80.
- [35] Wang ZJ, Russell D. Effect of forewing and hindwing interactions on aerodynamic forces and power in hovering dragonfly flight. *Physical Review Letters* 2007;99(14):148101.
- [36] Sun M, Lan SL. A computational study of the aerodynamic forces and power requirements of dragonfly (*Aeshna juncea*) hovering. *Journal of Experimental Biology* 2004;207(11):1887–901.
- [37] Lan S, Sun M. Aerodynamic force and flow structures of two airfoils in flapping motions. *Acta Mechanica Sinica* 2001;17(4):310–31.
- [38] Isogai K, Fujishiro S, Saitoh T, Yamamoto M, Yamasaki M, Matsubara M. Unsteady three-dimensional viscous flow simulation of a dragonfly hovering. *AIAA Journal* 2004;42(10):2053–9.
- [39] Warkentin J, DeLaurier J. Experimental aerodynamic study of tandem flapping membrane wings. *Journal of Aircraft* 2007;44(5):1653–61.
- [40] Saharon D, Luttges M. Three-dimensional flow produced by a pitching-plunging model dragonfly wing. In: Proceedings of 25th AIAA aerospace sciences meeting; 1987.
- [41] Saharon D, Luttges M. Visualization of unsteady separated flow produced by mechanically driven dragonfly wing kinematics model. In: Proceedings of 26th AIAA aerospace sciences meeting; 1988.
- [42] Saharon D, Luttges M. Dragonfly unsteady aerodynamic: the role of the wing phase relations in controlling the produced flows. In: Proceedings of 27th AIAA aerospace sciences meeting; 1989.
- [43] Akhtar I, Mittal R, Lauder G, Drucker E. Hydrodynamics of a biologically inspired tandem flapping foil configuration. *Theoretical and Computational Fluid Dynamics* 2007;21(3):155–70.
- [44] Sun M, Huang H. Dragonfly forewing-hindwing interaction at various flight speeds and wing phasing. *AIAA Journal* 2007;45(2):508–11.
- [45] Wang JK, Sun M. A computational study of the aerodynamics and forewing-hindwing interaction of a model dragonfly in forward flight. *Journal of Experimental Biology* 2005;208(19):3785–804.
- [46] Broering T, Lian Y, Henshaw W. Numerical investigation of energy extraction in a tandem flapping wing configuration. *AIAA Journal* 2012;50:2295–308.
- [47] Rival D, Hass G, Tropea C. Recovery of energy from leading- and trailing-edge vortices in tandem-airfoil configurations. *Journal of Aircraft* 2011;48(1):203–11.
- [48] Rival D, Schönweitz D, Tropea C. Vortex interaction of tandem pitching and plunging plates: a two-dimensional model of hovering dragonfly-like flight. *Bioinspiration & Biomimetics* 2011;6(1):016008.
- [49] Lim KB, Tay WB. Numerical analysis of the s1020 airfoils in tandem under different flapping configurations. *Acta Mechanica Sinica* 2010;26:191–207.
- [50] Broering TM, Lian Y-S. The effect of phase angle and wing spacing on tandem flapping wings. *Acta Mechanica Sinica* 2012;28(6):1557–71.
- [51] Kumar AG, Hu H. An experimental investigation on the wake flow characteristics of tandem flapping wings; 2011.
- [52] Jones KD, Lund TC, Platzer MF. Experimental and computational investigation of flapping wing propulsion for micro air vehicles. *Prog. Astronaut. Aeronaut.* 2001;195:307–39.
- [53] Zhang G. Unsteady aerodynamics of a morphing tandem wing UAV. *Journal of Aircraft* 2012;49:5.
- [54] English TG, Simpson JR, Landman D, Parker PA. An efficient split-plot approach for modeling nonlinear aerodynamic effects. *Quality Engineering* 2012;24(4):522–30.
- [55] Dong H, Liang Z. Effects of ipsilateral wing-wing interactions on aerodynamic performance of flapping wings. *AIAA Pap.* 2010:2010–71.
- [56] Zhu Q, Wolfgang M, Yue D, Triantafyllo M. Three-dimensional flow structures and vorticity control in fish-like swimming. *Journal of Fluid Mechanics* 2002;468:1–28.
- [57] Carpenter P, Locke N. Investigation of wind speeds over multiple two-dimensional hills. *Journal of Wind Engineering and Industrial Aerodynamics* 1999;83(1–3):109–20.
- [58] Dutt AJ. Wind flow in an urban environment. *Environmental Monitoring and Assessment* 1991;19(1–3):495–506.
- [59] Kastner-Klein P, Fedorovich E, Ketzel M, Berkowicz R, Britter R. The modelling of turbulence from traffic in urban dispersion models—Part II: evaluation against laboratory and full-scale concentration measurements in street canyons. *Environmental Fluid Mechanics* 2003;3(2):145–72.
- [60] Vachon G, Louka P, Rosant JM, Mestayer PG, Sini JF. Measurements of traffic-induced turbulence within a street canyon during the Nantes'99 Experiment. *Water, Air, & Soil Pollution: Focus* 2002;2(5–6):127–40.
- [61] Rizzetta DP, Visbal MR. Exploration of plasma-based control for low-Reynolds number airfoil/gust interaction. *International Journal of Computational Fluid Dynamics* 2011;25(10):509–33.
- [62] Lian Y, Shyy W. Laminar-turbulent transition of a low Reynolds number rigid or flexible airfoil. *AIAA Journal* 2007;45(7):1501.
- [63] Kerstens W, Pfeiffer J, Williams D, King R, Colonius T. Closed-loop control of lift for longitudinal gust suppression at low Reynolds numbers. *AIAA J.* 2011;49(8):1721–8.
- [64] Golubev VV, Dreyer BD, Visbal MR, Golubev NV. High-accuracy viscous simulation of gust interaction with stationary and pitching wing sections. *AIAA Pap.* 2009:2009–11.
- [65] Lap N, Vladimir G, Jonathan D, Miguel V. High-fidelity simulations of transitional airfoil interacting with canonical upstream flow disturbances. In: 42nd AIAA fluid dynamics conference and exhibit. Fluid dynamics and co-located conferences. American Institute of Aeronautics and Astronautics; 2012.
- [66] Prater R, Lian Y. Aerodynamic response of stationary and flapping wings in oscillatory low Reynolds number flows; 2012.
- [67] Gad-el-Hak M. Micro-air-vehicles: can they be controlled better? *Journal of Aircraft* 2001;38:419–29.
- [68] Rees CJ. Aerodynamic properties of an insect wing section and a smooth airfoil compared. *Nature* 1975;258(5531):141–2.
- [69] Rudolph R. Aerodynamic properties of *Libella quadrimaculata* L. (Anisoptera, Libellulidae), and the flow around smooth and corrugated wing section models during gliding flight. *Odonatologica* 1987;7:49–58.
- [70] Kesel AB. Aerodynamic characteristics of dragonfly wing sections compared with technical airfoils. *Journal of Experimental Biology* 2000;203(20):3125–35.
- [71] Murphy J, Hu H. An experimental investigation on a bio-inspired corrugated airfoil. In: 47th AIAA aerospace sciences meeting including the new horizons forum and aerospace exposition. Aerospace sciences meetings. American Institute of Aeronautics and Astronautics; 2009.
- [72] Vargas A, Mittal R, editors. Aerodynamic performance of biological airfoils. In: 2nd AIAA flow control conference. AIAA paper; 2004.
- [73] Kim W-K, Ko JH, Park HC, Byun D. Effects of corrugation of the dragonfly wing on gliding performance. *Journal of Theoretical Biology* 2009;260(4):523–30.

- [74] Sunada S, Yasuda T, Yasuda K, Kawachi K. Comparison of wing characteristics at ultralow Reynolds number. *Journal of Aircraft* 2002;39(2):331–8.
- [75] Kesel AB, Philippi U, Nachtigall W. Biomechanical aspects of the insect wing: an analysis using the finite element method. *Computers in Biology and Medicine* 1998;28(4):423–37.
- [76] Hord K, Lian Y. Numerical investigation of the aerodynamic and structural characteristics of a corrugated airfoil. *Journal of Aircraft* 2012;49(3):749–57.
- [77] Henshaw WD, Petersson NA. A split-step scheme for the incompressible Navier–Stokes equations. *Numerical simulations of incompressible flows* 2001;2003:108–25.
- [78] Balay WDG S, McInnes LC, Smith BF. The portable extensible toolkit for scientific computation. Argonne National Laboratory; 1999. Available from: <<http://www.mcs.anl.gov/petsc/petsc.html>>.
- [79] Young J. Numerical simulation of the unsteady aerodynamic flapping airfoils [Ph.D. thesis]. The University of New South Wales/Australian Defence Force Academy; 2005.
- [80] Young J, Lai JC S, Germain C. Simulation and parameter variation of flapping-wing motion based on dragonfly hovering. *AIAA Journal* 2008;46(4):918–24.
- [81] Lian Y, Shyy W. Aerodynamics of low Reynolds number plunging airfoil under gusty environment. AIAA Paper 2007-71. In: 45th AIAA aerospace sciences meeting and exhibit 2007.
- [82] OI M. Unsteady aerodynamics for micro air vehicles; 2010.
- [83] Henshaw WD, Schwendeman DW. Moving overlapping grids with adaptive mesh refinement for high-speed reactive and non-reactive flow. *Journal of Computational Physics* 2006;216(2):744–79.
- [84] McCroskey WJ, Carr LW, McAlister KW. Dynamic stall experiments on oscillating airfoils. *AIAA Journal* 1976;14(1):57–63.
- [85] Visbal M, Shang J. Investigation of the flow structure around a rapidly pitching airfoil. *AIAA Journal* 1989;27(8):1044–51.
- [86] Liu H, Kawachi KA. Numerical study of insect flight. *Journal of Computational Physics* 1998;146(1):124–56.
- [87] Wakeling J, Ellington C. Dragonfly flight. II. Velocities, accelerations and kinematics of flapping flight. *Journal of Experimental Biology* 1997;200(3):557–82.
- [88] Azuma A, Azuma S, Watanabe I, Furuta T. Flight mechanics of a dragonfly. *Journal of Experimental Biology* 1985;116(1):79–107.
- [89] Jones KD, Bradshaw CJ, Papadopoulos J, Platzer MF. Bio-inspired design of flapping-wing micro air vehicles. *The Aeronautical Journal* 2005;109(1098):385–93.
- [90] Broering T, Lian Y-S. The effect of phase angle and wing spacing on tandem flapping wings. *Acta Mechanica Sinica* 2012;28(6):1557–71.
- [91] Taylor GK, Thomas ALR. Dynamic flight stability in the desert locust *Schistocercagregaria*. *Journal of Experimental Biology* 2003;206:2803–29.
- [92] Zhang Y-L, Wu J-H, Sun M. Lateral dynamic flight stability of hovering insects: theory vs. numerical simulation. *Acta Mechanica Sinica* 2012;28(1):221–31.
- [93] Nagai H, Isogai, T, Fujimoto, T. Experimental study on flow interaction between fore- and hindwings of dragonfly in hovering and forward flight. In: 27th Congress of International Council of the Aeronautical Sciences; 2004.
- [94] SolidWorks 2009. Concord, Massachusetts, USA.
- [95] Jones K, Platzer M. Time-domain analysis of low-speed airfoil flutter. *AIAA Journal* 1996;34(5):1027–33.